Curvature-induced Zn 3d electron return on Zn-N4 single-atom carbon nanofibers for boosting electroreduction of CO2

ChemCatChem

The European Society Journal for Catalysis

Chemistry Europe

European Chemical Societies Publishing

Supported by GECATS GERMAN CATALYSIS SOCIETY

Accepted Article

Title: Curvature-induced Zn 3d Electron Return on Zn-N4 Single-atom Carbon Nanofibers for Boosting Electroreduction of CO2

Authors: Mingwei Fang, Xingpu Wang, Xueyan Li, Ying Zhu, Guozheng Xiao, Jingjing Feng, Xiaohui Jiang, Kuilin Lv, Ying Zhu, and Wen-Feng Lin

To be cited as: *ChemCatChem* 10.1002/cctc.202001667

Link to VoR: https://doi.org/10.1002/cctc.202001667

WILEY-VCH

Curvature-induced Zn 3d Electron Return on Zn-N_4 Single-atom Carbon Nanofibers for Boosting Electroreduction of CO_2

Mingwei Fang,[a] Xingpu Wang,[a] Xueyan Li,[a] Ying Zhu,[a] Guozheng Xiao,[a] Jingjing Feng,[a] Xiaohui Jiang,[a] Kuilin Lv,[a] Ying Zhu,*[a][b] and Wen-Feng Lin*[c]

[a] M. Fang, X. Wang, X. Li, Y. Zhu, G. Xiao, J. Feng, X. Jiang, K. Lv, Prof. Y. Zhu
Key Laboratory of Bio-Inspired Smart Interfacial Science and Technology of Ministry of Education
School of Chemistry
Beihang University, Beijing 100191, China.
E-mail: zhuying@buaa.edu.cn (Prof. Y. Zhu), w.lin@lboro.ac.uk (Prof. W. F. Lin).
[b] Prof. Y. Zhu
Beijing Advanced Innovation Center for Biomedical Engineering
Beihang University, Beijing 100191, China.
[c] Prof. W. F. Lin
Department of Chemical Engineering
Loughborough University, Loughborough, Leicestershire LE11 3TU, U.K.

Supporting information for this article is given via a link at the end of the document.

Abstract: The electrochemical CO_2 reduction to desired chemical feedstocks is of importance, yet it is still challenging to obtain high production selectivity with low overpotential at a current density surpassing the industry benchmark of 100 mA cm^{-2}. Herein, we constructed a low-cost Zn single-atom anchored on curved N-doped carbon nanofibers (Zn SAs/N-C) by a facile noncovalent self-assembly approach. At a low overpotential of only 330 mV, the Zn SAs/N-C exhibited simultaneously both a high current density up to 121.5 mA cm^{-2} and a CO FE of 94.7%, superior to the previous reports. Experiments and DFT calculations revealed that the Zn atoms in Zn-N_4 acted as the active sites, while adjacent pyridine-N coupled with Zn-N_4 could synergistically decrease the free energy barrier for intermediate *COOH formation. Importantly, the curvature of catalyst induced Zn 3d electrons that were bound to the Zn-N bonds to return to Zn atom, thereby leading to an increase in electron density of Zn and accelerating CO_2 electroreduction to CO.

Introduction

The electrochemical CO_2 reduction reaction (CO_2RR) to produce value-added chemicals using renewable electricity has been widely considered as a promising approach for mitigating carbon emissions.[1] Nevertheless, CO_2RR generally involves multiple proton-coupled electron transfers and competing hydrogen evolution reaction (HER), thereby resulting in poor product selectivity and low conversion efficiency.[2] To meet the needs of practical application, this reduction reaction must achieve both high production selectivity and current density at low overpotentials.[3]

Over the past decades, a variety of electrocatalysts have been extensively developed for CO_2RR,[2c, 4] among which precious metal-based catalysts are the most efficient at low overpotentials. For example, Au-based catalysts showed high CO Faradaic efficiency (FE > 90%) with moderate current density (> 10 mA cm^{-2}) at low overpotentials (< 300 mV),[4b, 5] but they suffer from limited reserves and high cost. Recently, non-precious metal-based catalysts have been reported, yet typically exhibit a lower CO_2RR activity. Since being proposed by Zhang et al. in 2011,[6] the single atom catalysts (SACs) have attracted increasing interests due to their incredible catalytic performances and maximized atom utilization efficiency.[7] Especially, the SACs are capable of efficient CO_2 electroreduction to CO with excellent activity and selectivity, as well as superior stability, deriving from the optimal binding strength between single-atom active sites and the chemical species involved in CO_2RR.[8] For instance, single-atom dispersed Fe sites on N-doped carbon exhibited a high activity toward CO production with a FE of over 90% and a current density of 94 mA cm^{-2} at an overpotential of 340 mV in flow-type cell.[9] In a recent study, self-supported single-atom Ni carbon membrane catalyst achieved a high current density of more than 300 mA cm^{-2} with a CO FE of 88% at -1.0 V (vs RHE) in flow-type cell.[3b] Despite advances in individual metrics, large overpotentials (>500 mV) are required to reach commercially relevant current density (>100 mA cm^{-2}).[10] Thus, the catalytic activity of SACs still has much room for improvement, especially stable and highly selective production with lower overpotentials at a high current density.

As reported previously, the tip, corner and edge sites of catalysts often possess a higher catalytic activity.[4f, 11] For example, Sargent's group reported that gold or palladium nanoneedle electrocatalysts produced local high electric fields at the sharp tip that lead to a high local concentration of CO_2 close to the active CO_2 reduction reaction surface, which improved the efficiency of CO_2 reduction.[1c] Chai et al. demonstrated that the structural curvature can effectively improve the CO_2RR activity and selectivity of carbon-nanotube (CNT) catalysts via DFT calculations.[12] Moreover, Liu et al. found that a tip-enhanced local electric field at the Pt site on the curved carbon support could promote the reaction kinetics for hydrogen evolution.[13] As far as we know, however, the regulating electronic structure of single-atom sites by structural engineering for CO_2RR has been rarely reported.

Inspired by these works, we set out to utilize highly curved carbon supports for metal single-atom catalysts to improve the CO_2RR activity. Herein, we develop an ultrathin Zn single-atom layer anchored on curved N-doped carbon nanofibers (Zn SAs/N-C) by a facile self-assembly method and pyrolysis of the core-shell structural Zn (II) coordination polymers with 4,4'-bipyridine/polyaniline (PANI) nanofibers. The as-prepared Zn SAs/N-C acted as CO_2RR catalyst achieved simultaneously both

a high current density up to 121.5 mA cm^{-2} and a CO FE of 94.7% at a low overpotential of only 330 mV in flow-type cell, superior to the catalysts reported previously. Experimental and DFT studies revealed that Zn atoms of Zn-N_4 acted as the active sites for electroreduction of CO_2 to CO, and the adjacent pyridine-N had a synergistic effect with Zn-N_4 to lower the free energy barrier for *COOH formation. Importantly, Zn 3d electrons of Zn-N_4 sites that are generally bound to Zn-N bonds can return to Zn atom by a curvature-induced electron transfer that increase Zn electron density, thereby enhancing catalytic activity of CO_2 electroreduction to CO.

Results and Discussion

Preparation and Characterization of Zn SAs/N-C

The schematic illustration of the synthetic process for Zn SAs/N-C catalyst was shown in Figure 1a. PANI nanofibers were firstly fabricated by chemical oxidative polymerization of aniline, which acted directly as N and C sources, as well as hard template. The Zn (II) coordinated with 4,4'-bipyridine was self-assembled on the surface of PANI nanofibers by π-π interactions in aqueous reaction. After pyrolysis, Zn atoms would be atomically dispersed on N-doped carbon nanofibers. It was found that the morphologies and compositions of Zn SAs/N-C catalysts were largely affected by the pyrolysis temperature and the mass ratios of 4,4′-bipyridine and PANI nanofibers (Supplementary Figure S1-S6). If the 4,4′-bipyridine contents were too high or too low, the nanofiber structures could not be obtained, as shown in Supplementary Figure S2.

When the pyrolysis temperature was up to 1100°C, the Zn atoms in the catalyst were evaporated away due to the low boiling point of Zn. However, if the pyrolysis temperature was lower than 900°C, the obtained catalyst exhibited a low reduced activity, as shown in Supplementary Figure S3. Thus, an optimized Zn SAs/N-C catalyst was obtained at 1000°C with a mass ratio of 1:5 between 4,4′-bipyridine and PANI nanofibers. For a comparison, Zn-N-C and N-C catalysts were also prepared by direct pyrolysis of Zn (II) coordinated with 4,4′-bipyridine or PANI nanofibers under the same procedure as that for Zn SAs/N-C catalyst. It was found that the Zn-N-C catalyst was prone to aggregate to form larger nanoparticles, while the N-C catalyst could not maintain the morphology of initial nanofibers after pyrolysis (Supplementary Figure S7-S8). By contrast, the as-prepared Zn SAs/N-C catalyst retained the morphology of nanofibers after pyrolysis (Figure 1b). As shown in high resolution TEM (HRTEM) in Figure 1c, no particles or clusters were observed on the surface of Zn SAs/N-C nanofibers, which displayed an ultra-thin shell thickness of about 2-3 nm. The high-angle annular dark field-scanning transmission electron microscopic image (HADDF-STEM, Figure 1d) showed clearly high-density bright dots on the surface of nanofibers, these dots were assigned to Zn single atoms. In addition, the existence of Zn single atoms was further verified by the intensity profile along the line X-Y in HAADF-STEM image, as shown in Figure 1e, where the signal intensity is approximately proportional to the square of atomic number. Inductively coupled plasma mass spectrometric (ICP-MS) result indicated that the mass loading of Zn on N-C was about 0.13 wt%, which corresponded to the amount of Zn in the precursors. X-ray diffraction (XRD) was used to characterize the crystal structure of the catalysts. As can be seen from Figure 2a, the Zn SAs/N-C and N-C catalysts showed similar diffraction patterns with broad graphite peaks, implying the absence of Zn nanoparticles, which is consistent with the SEM, HRTEM and HAADF-STEM results. The graphitic structures of Zn SAs/N-C, Zn-N-C and N-C were also investigated by Raman spectroscopy (Supplementary Figure S9). In all the spectra recorded, two peaks around 1580 and 1348 cm^{-1} were observed, which assigned to the stretching vibrations of sp^2-bonded (G-bond) carbon and defect-induced breathing mode of aromatic ring (D bond), respectively.[14]

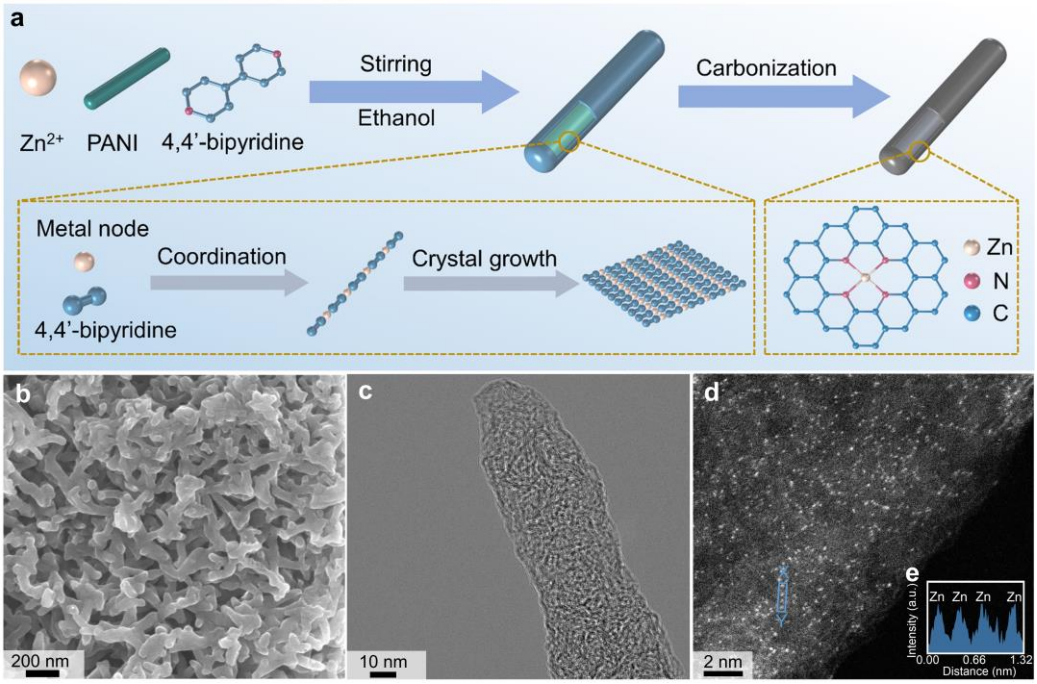

Figure 1. (a) Schematic illustration of the formation of Zn SAs/N-C. (b) SEM image of Zn SAs/N-C. (c) High resolution TEM (HRTEM) image of Zn SAs/N-C. (d) HAADF-STEM image of Zn SAs/N-C. (e) The inset is the corresponding intensity profiles along the line X–Y in (d).

The defect density was quantified by the intensity ratio of the D and G bonds (I_D/I_G),[15] it was therefore found that the degree of graphitization of Zn SAs/N-C is higher than those of Zn-N-C and N-C, indicating that Zn SAs/N-C had a better electron transfer capability. To elucidate the elemental composition and related chemical states, X-ray photoelectron spectroscopy (XPS) data of catalysts were collected (Supplementary Figure S3 and S10), which indicated the presence of C, N, Zn elements in Zn SAs/N-C. The high-resolution N 1s XPS spectrum of Zn SAs/N-C (Figure 2 b) can be deconvoluted into five peaks associated with pyridinic-N (398.4 eV), Zn-N (399.6 eV), pyrrolic-N (400.5 eV), graphitic-N (401.4 eV), and oxidized-N (403.5 eV) species. As shown in Supplementary Figure S11, the Zn SAs/N-C had a higher content of pyridinic-N species (22.5 at%) than that of Zn-N-C (16.2 at%) and N-C (16.3 at%). The abundant pyridinic-N in the materials was demonstrated a high affinity to CO_2,[16] which is crucial for CO_2 activation. Furthermore, Zn 2p XPS spectrum of Zn SAs/N-C (Figure 2c) indicted clearly that two peaks located at 1021.3 and 1044.5 eV corresponded to the Zn $2p_{3/2}$ and Zn $2p_{1/2}$ states, respectively.[17] Notably, the binding energy for Zn $2p_{3/2}$ (1021.3 eV) is obviously lower than that of ZnO (1022.0 eV), indicating the presence of the Zn-N coordination bond in Zn SAs/N-C, rather than ZnO. N_2 adsorption-desorption isotherms (Supplementary Figure S12a) show that Zn SAs/N-C had a Burnauer-Emmett-Teller surface of 25.39 m^2 g^{-1}, with an average pore diameter of 2.90 nm (Supplementary Figure S12b). Besides, CO_2 adsorption isotherms of the Zn SAs/N-C, Zn-N-C and N-C catalysts (Supplementary Figure S13) verify the excellent CO_2 capture capability of the Zn SAs/N-C, suggesting a better CO_2 access and transport in the porous structures.[18]

To further study the elemental environment of the catalysts, X-ray absorption near edge structure (XANES) and extended X-ray absorption fine structure (EXAFS) data were examined. The Zn K-edge XANES spectra of Zn SAs/N-C along with those of ZnO and Zn foil references were shown in Figure 2d. The near edge of Zn SAs/N-C was found to be in between that of Zn foil and ZnO, suggesting that the average valence state of Zn was an intermediate stage to Zn (0) and Zn (Ⅱ). Figure 2e displayed the Fourier transform (FT) k^2-weighted $\chi(k)$ function of the extended X-ray absorption fine structure (FT-EXAFS) of Zn SAs/N-C. It showed that only one peak at 1.7 Å assigned to the Zn-N coordination can be observed, but no Zn-Zn coordination peak (2.3 Å), thereby giving powerful evidence for the formation of single Zn atoms anchored on N_x sites. Wavelet transform (WT) was adopted to analyze Zn K-edge EXAFS oscillations, the WT maximum for the Zn SAs/N-C was found at 5.5 $Å^{-1}$ assigned to the Zn-N, but no Zn-Zn (7.2 $Å^{-1}$) observed, as compared with WT plots for Zn foil and ZnO in Figure 2h-i. Furthermore, EXAFS fitting was employed to acquire the chemical configuration of Zn atoms. As displayed in Figure 2f and Supplementary Table S1, the central Zn atom exhibited a coordination number of four with an average Zn-N bonds length of 1.98 Å, which are consistent with XPS results (Zn-N, 399.6 eV). All above-mentioned results provide strong evidences that Zn SAs/N-C with atomically dispersed Zn bonded with four N atoms to form Zn-N_4 sites was successfully synthesized.

Electrocatalytic Performances toward CO_2RR

The electrocatalytic activities of Zn SAs/N-C, Zn-N-C and N-C catalysts for CO_2RR were studied using a three-electrode H-cell with CO_2- or N_2-saturated 0.5 M $KHCO_3$ solution as the

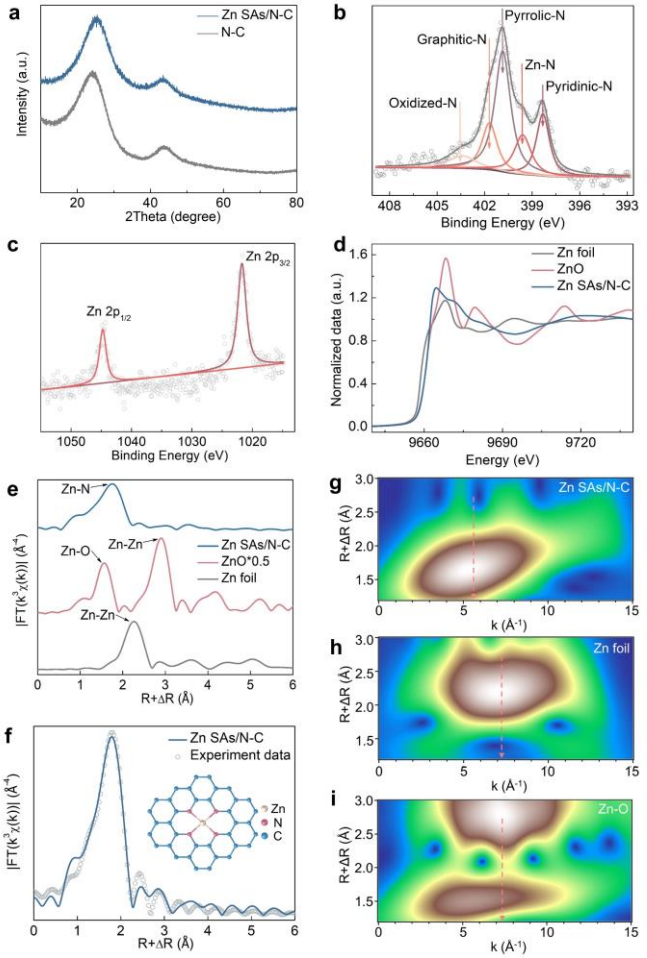

Figure 2. Characterizations of Zn SAs/N-C. (a) XRD patterns. (b) High-resolution N 1s spectra of Zn SAs/N-C. (c) High-resolution Zn 2p spectra of Zn SAs/N-C. (d) Zn K-edge XANES spectra of Zn SAs/N-C, ZnO and Zn foil. (e) Fourier transforms of the k^2-weighted χ(k) functions of the EXAFS spectra for the Zn K-edge. (f) A typical EXAFS fitting curve in R space of Zn SAs/N-C (inset shows a model of the Zn environment). (g-i) WT-EXAFS of Zn SAs/N-C (g), Zn foil (h), and ZnO (i).

electrolyte. As the catalytic reaction proceeded, only CO and H_2 gases were detected, and no liquid product was detected by H1 nuclear magnetic resonance spectroscopy. As described by the linear sweep voltammetry (LSV) (Supplementary Figure S14), for Zn SAs/N-C catalyst, a higher reduction current density at the onset potential around -0.16 V (vs RHE) was obtained in the CO_2-saturated electrolyte, revealing the significant electrocatalytic activity towards CO_2RR. Moreover, Zn SAs/N-C catalyst yielded the highest total current density compared to Zn-N-C and N-C catalysts (Figure 3a). For instance, the Zn SAs/N-C catalyst exhibited current densities of -11.29 mA cm^{-2} at -0.44 V (vs RHE) and -43.85 mA cm^{-2} at -0.90 V (vs RHE), respectively, exceeding those of Zn-N-C and N-C catalysts. Figure 3b showed the partial current density for CO formation (j_{CO}) as a function of the applied potential. At -0.44 V (vs RHE), Zn SAs/N-C catalyst achieved a high j_{CO} of 10.45 mA cm^{-2}, which was 2.0 and 5.4 times higher than those of Zn-N-C and N-C catalysts, respectively. Compared with Zn-N-C and N-C, Zn SAs/N-C obtained a maximum CO FE of 92.6% at an overpotential of 330 mV (Figure 3c). It should be emphasized that achieving high FE with moderate j_{CO} at such a low overpotential stood for a better energy conversion efficiency (Supplementary Table S2 and Supplementary Figure S15).[19] The intrinsic activity of Zn SAs/N-C catalyst was disclosed by the calculation of the TOF based on the j_{CO}. As shown in Figure 3d,

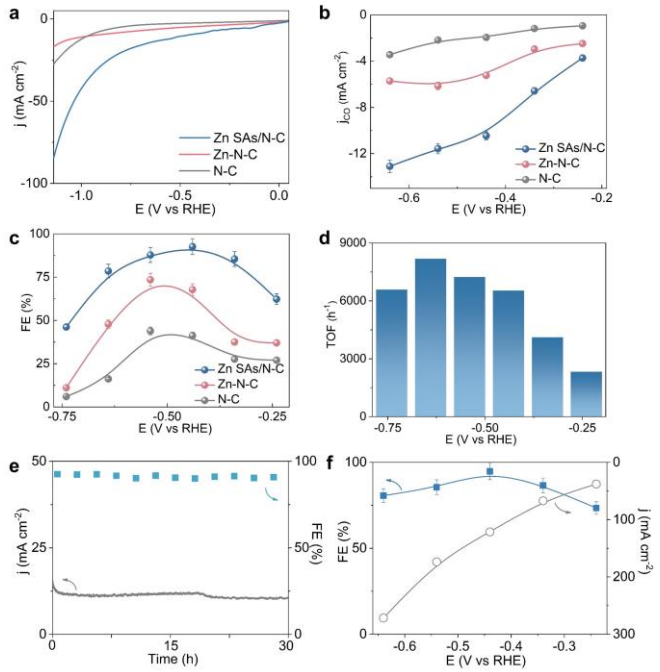

Figure 3. Electrochemical CO_2 reduction performances of catalysts in CO_2-saturated 0.5 M $KHCO_3$ aqueous solution. (a) LSV curves of Zn SAs/N-C, Zn-N-C, and N-C. (b) Partial current density of CO formation (jCO) for Zn SAs/N-C, Zn-N-C, and N-C. (c) FE of CO formation at different applied potentials. (d) TOFs of Zn SAs/N-C at different applied potentials. (e) Chronoamperometry curve and FE of CO production by Zn SAs/N-C at -0.44 V (vs RHE) over 30 hours. (f) FE of CO production and current densities at different applied potentials in flow-type cell.

Zn SAs/N-C has a large TOF of 8190 h^{-1} at -0.64 V (vs RHE), showing an excellent activity. On the other hand, the long-term activity test was performed to evaluate the stability of Zn SAs/N-C catalyst, which is another important parameter for the practical application. The Zn SAs/N-C catalyst showed almost no attenuation of the current density and the CO FE maintained over 30 hours (Figure 3e), showing an excellent durability. After 30 h test of CO_2RR, the Zn SAs/N-C catalyst was further characterized by SEM, XRD, Raman, and XPS. The results showed that the structure and metal valence state of catalyst didn't change significantly after and before test, indicating that the Zn SAs/N-C catalyst had high chemical stability (Supplementary Figure S16). The CO_2RR performance of Zn SAs/N-C catalyst was further assessed by using flow-type cell (Supplementary Figure S17). As shown in Figure 3f, Zn SAs/N-C displayed simultaneously a high current density of 121.5 mA cm^{-2} and CO FE of 94.7% at a low overpotential of only 330 mV, which outperformed the previous reports (Supplementary Table S3 and Supplementary Figure S18). Also, at current density of up to 271.8 mA cm^{-2} at -0.64 V (vs RHE), the FE for CO formation was still as high as over 80%. Moreover, it showed a stable current density around 120 mA cm^{-2} at -0.44 V (vs RHE) with a high CO selectivity of over 90% after 4 h continuous reaction (Supplementary Figure S19). To understand the high electrocatalytic activity of Zn SAs/N-C catalyst, the electrochemical active surface area (ECSA) determined by the Nyquist plots was then investigated. As measured, Zn SAs/N-C catalyst showed a high active surface area with a double layer capacitance of 7.22 mF cm^{-2}, which was 1.2 and 2.2 times higher than those of Zn-N-C and N-C catalysts, respectively (Supplementary Figure S20-22). Meanwhile, the lower charge-transfer resistant (R_{ct}) value of Zn SAs/N-C was assigned to the improved conductivity, thus facilitating charge-transfer process during CO_2RR, as shown in Supplementary Figure S23.[20] In addition, Tafel slopes for catalysts were measured to study the kinetics of electroreduction of CO_2. As shown in Supplementary Figure S24, the Tafel slopes of Zn SAs/N-C, Zn-N-C and N-C catalysts were obtained as 112, 140 and 150 mV dec^{-1}, respectively, which were consistent with a rate-determining initial electron transfer to CO_2 to form the adsorbed *COOH intermediate that was commonly appealed for metal-based electrodes.[21]

To prove the curvature effect, carbon nanotube-supported Zn SAs (Zn SAs/CNTs) and graphene-supported Zn SAs (Zn SAs/G) were also prepared respectively under the same conditions as for Zn SAs/N-C. As shown in Supplementary Figure S25, the Zn SAs/CNTs showed a CO FE of 82.6% at -0.44 V (vs RHE), which is higher than that of Zn SAs/G (60.1% at -0.44 V (vs RHE)), but lower than that of Zn SAs/N-C, suggesting that the curvature played an important role in improving the CO_2RR performance. Furthermore, to shed light on the active sites for CO_2 electroreduction to CO, the correlation between the N contents for different N species (pyridinic-N, Zn-N, pyrrolic-N, graphitic-N and oxidized-N) and the maximum CO FEs was investigated. As shown in Supplementary Figure S26, the linear scaling relationships between the pyridinic-N or Zn-N contents and the maximum CO FEs were obtained, respectively, whereas no clear trends could be observed for other N contents, indicating that pyridinic-N and Zn-N_4 sites were the most likely active sites for CO formation. Similarly, as given in Supplementary Figure S27, there was a linear relationship between the CO FEs of Zn SAs/N-C and the Zn SAs contents, further proving the importance of Zn atoms for CO_2RR. It has been proved previously that the selective adsorption of phosphate anion on pyridinic-N inhibited its catalytic activity.[22] Therefore, Zn SAs/N-C was soaked in 1 M phosphoric acid for 30 min before testing (denoted as Zn SAs/N-C-P). As shown in Supplementary Figure S28, the Zn SAs/N-C-P showed a CO FE of only 72.4% at -0.44 V (vs RHE), which was lower than that of Zn SAs/N-C, indicating that pyridine-N played an important role for electroreduction of CO_2 to CO. Furthermore, to distinguish the contribution of Zn-N_4, cyanide ion was adopted selectively to poison Zn-N_4 sites (denoted as Zn SAs/N-C-CN).[23] It can be seen that the Zn SAs/N-C-CN showed a CO FE of 63.4% at -0.44 V (vs RHE), which was significantly lower than that of Zn SAs/N-C. When both pyridine-N and Zn-N_4 in Zn SAs/N-C were inhibited at the same time (denoted as Zn SAs/N-C-PCN), the as-treated Zn SAs/N-C-PCN showed the lowest CO FE (43.7% at -0.44 V (vs RHE)) compared with that of Zn SAs/N-C-P and Zn SAs/N-C-CN. These results demonstrated that both Zn-N_4 and pyridine-N species of Zn SAs/N-C acted as active sites to synergistically enhance the catalytic reduction of CO_2 to CO.

DFT Calculations and Reaction Mechanism

To understand the mechanism of electroreduction of CO_2 to CO on Zn SAs/N-C, density functional theory (DFT) calculations were performed. The proposed reaction pathways for electroreduction of CO_2 to CO on Zn SAs/N-C are shown in Figure 4a: the electroreduction of CO_2 to CO generally involves two consecutive proton-electron coupled steps to form two intermediates of *COOH and *CO. In addition, considering the possible presence of doped N atoms near Zn-N_4, the free energy changes of pyridine-N, pyrrole-N, and graphite-N coupled with Zn-N_4 were all investigated, which were denoted as PD-Zn-N_4-X, PL-Zn-N_4-X and GN-Zn-N_4-X, where X=1, 2 and 3 that represent the

different relative positions of Zn-N_4 and N, as shown in Supplementary Figure S29-S31 and Supplementary Table S4-S9.

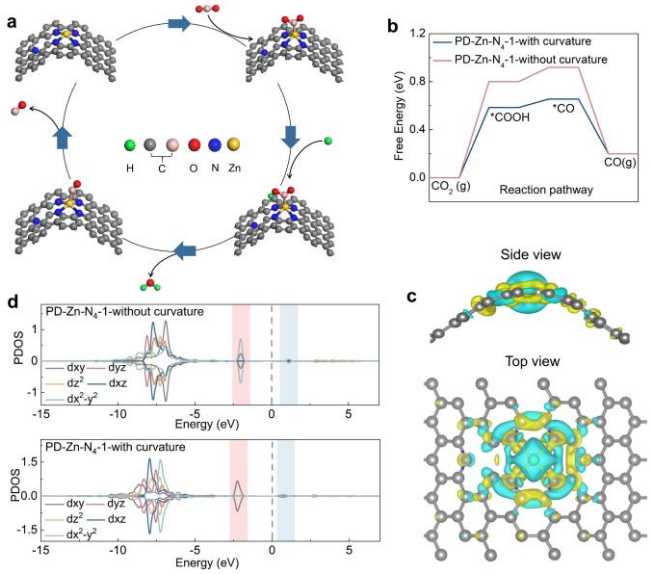

Figure 4. (a) The proposed reaction pathways for complete CO_2 reduction reaction on Zn SAs/N-C. (b) Free energy diagram for the conversion of CO_2 into CO at U=0 V versus RHE on the PD-Zn-N_4-1-without and with curvature; PD represents pyridine-N coupled to Zn in the Zn-N_4, 1 represents that Zn-N_4 and N are adjacent in the horizontal direction, see the text for details. The proposed surface reaction mechanism involves the following steps: (1) $CO_2 + * + H^+ + e^- \rightarrow$ *COOH, (2) *COOH + $H^+ + e^- \rightarrow$ *CO + H_2O, (3) *CO $\rightarrow$ CO + *, where * denotes the adsorbed site on the catalyst surface. (c) Top and side views of differential charge density for PD-Zn-N_4-1-with curvature. The yellow and blue isosurfaces correspond to the increase in the number of electrons and the depletion zone, respectively. (d) Partial density of state (PDOS) of d orbital in Zn atom for PD-Zn-N_4-1-without and -with curvature.

The calculated results indicate that the Zn atoms in Zn-N_4 was the active sites and the PD-Zn-N_4-1 had the lowest free energy barrier for the intermediate *COOH formation due to a synergistic effect between the adjacent pyridine-N and Zn-N_4, compared with all other structures, thus improving the activity towards CO_2 electroreduction to CO, which were well consistence with the experimental results. Meanwhile, curvature effect on catalytic activity was further studied on the optimum catalyst PD-Zn-N_4-1-without and -with curvature, respectively, as presented in Figure 4b. It was found that the PD-Zn-N_4-1-with curvature showed a significantly lower free energy barrier for the aforementioned rate-determining step, compared to that of PD-Zn-N_4-1-without curvature, indicating that the curvature of the catalyst indeed improved its catalytic activity for CO_2 electroreduction to CO.

To further clarify the curvature role, the differential charge density and partial density of state (PDOS) of PD-Zn-N_4-1-without and with curvature were investigated carefully. It was found that both PD-Zn-N_4-1-without and -with curvature (Figure 4c and Supplementary Figure S32) possessed mushroom-like charge density distribution on the Zn atom (blue color corresponds to the depletion zone), which were similar with the previous reports.[24] However, the calculated bader charge results showed that Zn atom on PD-Zn-N_4-1-with curvature displayed a lower positive charge than that of PD-Zn-N_4-1-without curvature (Supplementary Figure S33 and Supplementary Table S10), indicating that the curvature induced an increase in the electron density of Zn atom. Furthermore, PDOS images also displayed an obvious difference between the two structures, as shown in Figure 4d. The d_{xy} and $d_{x^2-y^2}$ orbital electrons of Zn atom in PD-Zn-N_4-1-without curvature were located around the Fermi level, that was, between the bonding state (2 eV below the Fermi level) and anti-bonding state (1 eV above the Fermi level), suggesting that the electrons on these two d orbitals were tightly bound to Zn-N bonds. As the curvature was introduced, however, the $d_{x^2-y^2}$ orbital electron of Zn atom in PD-Zn-N_4-1-with curvature disappeared from the Fermi level region and shifted to the lower energy region between -10 and -5 eV, indicating that the $d_{x^2-y^2}$ orbital electron of Zn atom was released from Zn-N bonds to return to Zn atom, thus increasing the electron density of Zn atom that promoted the electroreduction of CO_2 to CO.

Conclusion

We developed a low-cost yet highly efficient SACs catalyst for CO_2 electroreduction to CO, which consists of curved N-doped carbon nanofibers covered with an ultrathin layer of Zn SAs (Zn SAs/N-C), derived from the core-shell structural Zn (II) coordinated with 4,4'-bipyridine/PANI nanofibers via direct pyrolysis. The Zn SAs/N-C catalyst showed both high current density up to 121.5 mA cm^{-2} and CO FE of 94.7% at a low overpotential of only 330 mV in flow-type cell, which outperformed that of the reported catalysts. Further experiments and DFT calculations revealed that the Zn atoms in Zn-N_4 were the active sites for CO_2RR, and both Zn-N_4 and neighboring pyridine-N could synergistically lower the free energy barrier for *COOH formation. Importantly, the curvature of the nanofiber could induce the $d_{x^2-y^2}$ obrital electron of Zn atom being held by Zn-N bonds to return to Zn atom, thereby increasing the electron density of Zn and improving the activity toward CO_2 electroreduction to CO. This work not only provides a new perspective for the design of SACs, but also deepens the fundamental understanding of mechanism of CO_2 electroreduction at atomic levels.

Acknowledgements

The work is supported by the National Natural Science Foundation of China (51672019, 51872013), the National Key Research and Development Program of China (2017YFA0206902), the 111 Project (B14009), and the Royal Society and the Newton Fund (NAF\R1\191294).

Keywords: Electrochemical CO_2 reduction reaction • Zn single-atom catalyst • curvature-induced d electron return • curved N-doped carbon nanofibers

[1] a) B. Obama, *Science* **2017**, *355*, 126; b) B. A. Rosen, A. Salehi-Khojin, M. R. Thorson, W. Zhu, D. T. Whipple, P. J. A. Kenis, R. I. Masel, *Science* **2011**, *334*, 643; c) M. Liu, Y. Pang, B. Zhang, P. De Luna, O. Voznyy, J. Xu, X. Zheng, C. T. Dinh, F. Fan, C. Cao, F. P. G. de Arquer, T. S. Safaei, A. Mepham, A. Klinkova, E. Kumacheva, T. Filleter, D. Sinton, S. O. Kelley, E. H. Sargent, *Nature* **2016**, *537*, 382-386; d) S. Lin, C. S. Diercks, Y.-B. Zhang, N. Kornienko, E. M. Nichols, Y. Zhao, A. R. Paris, D. Kim, P. Yang, O. M. Yaghi, C. J. Chang, *Science* **2015**, *349*, 1208; e) S. Chu, Y. Cui, N. Liu, *Nat Mater* **2016**, *16*, 16-22.

[2] a) X. Li, W. Bi, M. Chen, Y. Sun, H. Ju, W. Yan, J. Zhu, X. Wu, W. Chu, C. Wu, Y. Xie, *J. Am. Chem. Soc.* **2017**, *139*, 14889-14892; b) D. Voiry, H. S. Shin, K. P. Loh, M. Chhowalla, *Nat. Rev. Chem.* **2018**, *2*, 0105; c) M. Asadi, K. Kim, C. Liu, A. V. Addepalli, P. Abbasi, P. Yasaei, P. Phillips, A. Behranginia, J. M. Cerrato, R. Haasch, P. Zapol, B. Kumar, R. F. Klie, J. Abiade, L. A. Curtiss, A. Salehi-Khojin, *Science* **2016**, *353*, 467; d) L.

Zhang, Z.-J. Zhao, J. Gong, *Angew. Chem. Int. Ed.* **2017**, *56*, 11326-11353.

[3] a) F. P. García de Arquer, C.-T. Dinh, A. Ozden, J. Wicks, C. McCallum, A. R. Kirmani, D.-H. Nam, C. Gabardo, A. Seifitokaldani, X. Wang, Y. C. Li, F. Li, J. Edwards, L. J. Richter, S. J. Thorpe, D. Sinton, E. H. Sargent, *Science* **2020**, *367*, 661; b) H. Yang, Q. Lin, C. Zhang, X. Yu, Z. Cheng, G. Li, Q. Hu, X. Ren, Q. Zhang, J. Liu, C. He, *Nat. Commun.* **2020**, *11*, 593.

[4] a) Z. Xia, M. Freeman, D. Zhang, B. Yang, L. Lei, Z. Li, Y. Hou, *ChemElectroChem* **2018**, *5*, 253-259; b) Y. Chen, C. W. Li, M. W. Kanan, *J. Am. Chem. Soc.* **2012**, *134*, 19969-19972; c) W. Ma, S. Xie, X.-G. Zhang, F. Sun, J. Kang, Z. Jiang, Q. Zhang, D.-Y. Wu, Y. Wang, *Nat. Commun.* **2019**, *10*, 892; d) K. L. Lv, W. Q. Suo, M. D. Shao, Y. Zhu, X. P. Wang, J. J. Feng, M. W. Fang, *Nano Energy* **2019**, *63*, 103834; e) X. Duan, J. Xu, Z. Wei, J. Ma, S. Guo, S. Wang, H. Liu, S. Dou, *Adv. Mater.* **2017**, *29*, 1701784; f) Y. Zhu, K. Lv, X. Wang, H. Yang, G. Xiao, Y. Zhu, *J. Mater. Chem. A* **2019**, *7*, 14895-14903.

[5] W. Zhu, Y.-J. Zhang, H. Zhang, H. Lv, Q. Li, R. Michalsky, A. A. Peterson, S. Sun, *J. Am. Chem. Soc.* **2014**, *136*, 16132-16135.

[6] B. Qiao, A. Wang, X. Yang, L. F. Allard, Z. Jiang, Y. Cui, J. Liu, J. Li, T. Zhang, *Nat. Chem.* **2011**, *3*, 634-641.

[7] a) Y. J. Chen, S. F. Ji, C. Chen, Q. Peng, D. S. Wang, Y. D. Li, *Joule* **2018**, *2*, 1242-1264; b) C. Zhao, X. Dai, T. Yao, W. Chen, X. Wang, J. Wang, J. Yang, S. Wei, Y. Wu, Y. Li, *J. Am. Chem. Soc.* **2017**, *139*, 8078-8081; c) H. B. Yang, S.-F. Hung, S. Liu, K. Yuan, S. Miao, L. Zhang, X. Huang, H.-Y. Wang, W. Cai, R. Chen, J. Gao, X. Yang, W. Chen, Y. Huang, H. M. Chen, C. M. Li, T. Zhang, B. Liu, *Nat. Energy* **2018**, *3*, 140-147; d) G. Zhang, Y. Jia, C. Zhang, X. Xiong, K. Sun, R. Chen, W. Chen, Y. Kuang, L. Zheng, H. Tang, W. Liu, J. Liu, X. Sun, W.-F. Lin, H. Dai, *Energy Environ. Sci.* **2019**, *12*, 1317-1325; e) N. Wang, Z. Liu, J. Ma, J. Liu, P. Zhou, Y. Chao, C. Ma, X. Bo, J. Liu, Y. Hei, Y. Bi, M. Sun, M. Cao, H. Zhang, F. Chang, H.-L. Wang, P. Xu, Z. Hu, J. Bai, H. Sun, G. Hu, M. Zhou, *ACS Sustain. Chem. Eng.* **2020**, *8*, 13813-13822.

[8] Q. Zhang, J. Guan, *Adv. Funct. Mater.* **2020**, *30*, 2000768.

[9] J. Gu, C.-S. Hsu, L. Bai, H. M. Chen, X. Hu, *Science* **2019**, *364*, 1091.

[10] D. Deng, K. S. Novoselov, Q. Fu, N. Zheng, Z. Tian, X. Bao, *Nat. Nanotechnol.* **2016**, *11*, 218-230.

[11] a) D. Tan, W. Lee, Y. E. Kim, Y. N. Ko, M. H. Youn, Y. E. Jeon, J. Hong, S. K. Jeong, K. T. Park, *ACS Sustainable Chemistry & Engineering* **2020**, *8*, 10639-10645; b) L. Fan, Z. Xia, M. Xu, Y. Lu, Z. Li, *Adv. Funct. Mater.* **2018**, *28*, 1706289; c) Y. Cheng, S. Zhao, H. Li, S. He, J.-P. Veder, B. Johannessen, J. Xiao, S. Lu, J. Pan, M. F. Chisholm, S.-Z. Yang, C. Liu, J. G. Chen, S. P. Jiang, *Appl. Catal. B: Environ.* **2019**, *243*, 294-303.

[12] G.-L. Chai, Z.-X. Guo, *Chem. Sci.* **2016**, *7*, 1268-1275.

[13] D. Liu, X. Li, S. Chen, H. Yan, C. Wang, C. Wu, Y. A. Haleem, S. Duan, J. Lu, B. Ge, P. M. Ajayan, Y. Luo, J. Jiang, L. Song, *Nat. Energy* **2019**, *4*, 512-518.

[14] H.-Y. Jeong, M. Balamurugan, V. S. K. Choutipalli, E.-s. Jeong, V. Subramanian, U. Sim, K. T. Nam, *J. Mater. Chem. A* **2019**, *7*, 10651-10661.

[15] H. Guo, Q. Feng, K. Xu, J. Xu, J. Zhu, C. Zhang, T. Liu, *Adv. Funct. Mater.* **2019**, *29*, 1903660.

[16] J. Wu, M. Liu, P. P. Sharma, R. M. Yadav, L. Ma, Y. Yang, X. Zou, X.-D. Zhou, R. Vajtai, B. I. Yakobson, J. Lou, P. M. Ajayan, *Nano Lett.* **2016**, *16*, 466-470.

[17] J. Li, S. Chen, N. Yang, M. Deng, S. Ibraheem, J. Deng, J. Li, L. Li, Z. Wei, *Angew. Chem. Int. Ed.* **2019**, *58*, 7035-7039.

[18] W. L. Li, N. Fechler, T. J. Bandosz, *Applied Catalysis B-Environmental* **2018**, *234*, 1-9.

[19] H. Wang, Y.-K. Tzeng, Y. Ji, Y. Li, J. Li, X. Zheng, A. Yang, Y. Liu, Y. Gong, L. Cai, Y. Li, X. Zhang, W. Chen, B. Liu, H. Lu, N. A. Melosh, Z.-X. Shen, K. Chan, T. Tan, S. Chu, Y. Cui, *Nat. Nanotechnol.* **2020**, *15*, 131-137.

[20] Z. Chen, K. Mou, S. Yao, L. Liu, *J. Mater. Chem. A* **2018**, *6*, 11236-11243.

[21] Z. Geng, Y. Cao, W. Chen, X. Kong, Y. Liu, T. Yao, Y. Lin, *Appl. Catal. B: Environ.* **2019**, *240*, 234-240.

[22] S. Liu, H. Yang, X. Huang, L. Liu, W. Cai, J. Gao, X. Li, T. Zhang, Y. Huang, B. Liu, *Adv. Funct. Mater.* **2018**, *28*, 1800499.

[23] F. Yang, P. Song, X. Liu, B. Mei, W. Xing, Z. Jiang, L. Gu, W. Xu, *Angew. Chem. Int. Ed.* **2018**, *57*, 12303-12307.

[24] X. Zu, X. Li, W. Liu, Y. Sun, J. Xu, T. Yao, W. Yan, S. Gao, C. Wang, S. Wei, Y. Xie, *Adv. Mater.* **2019**, *31*, 1808135.

Table of Contents

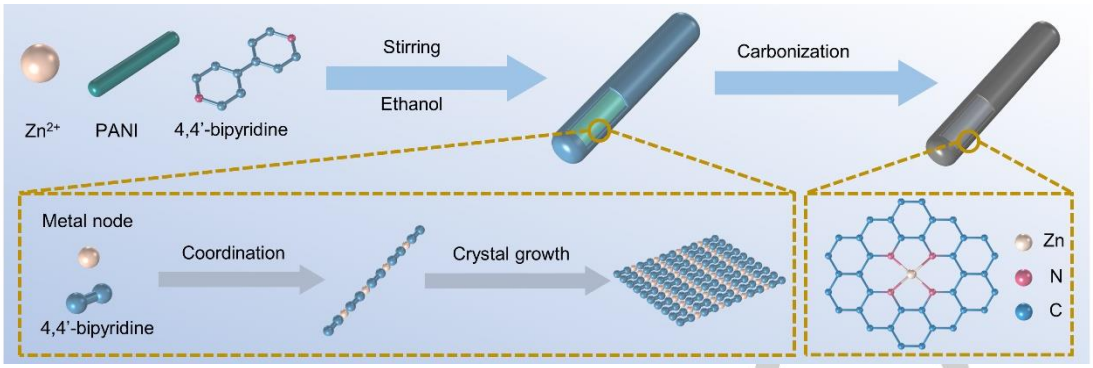

A Zn single-atom layer anchored on N-doped carbon nanofiber (Zn SAs/N-C) catalyst was developed by a self-assembly method. The Zn SAs/N-C achieved both a high current density of 121.5 mA cm^{-2} and a CO FE of 94.7% at a low overpotential of 330 mV. Further studies revealed that the adjacent pyridine-N had a synergistic effect with Zn-N_4. Zn 3d electrons that bound to Zn-N bonds could return to Zn atom by a curvature-induced electron transfer.

Supporting Information

Curvature-induced Zn 3d Electron Return on Zn-N_4 Single-atom Carbon Nanofibers for Boosting Electroreduction of CO_2

Mingwei Fang, Xingpu Wang, Xueyan Li, Ying Zhu, Guozheng Xiao, Jingjing Feng, Xiaohui Jiang, Kuilin Lv, Ying Zhu,* and Wen-Feng Lin*

Abstract: The electrochemical CO_2 reduction to desired chemical feedstocks is highly desirable, yet it is still challenging to obtain high selectivity and current density with low overpotential at the same time. Herein, we constructed a low-cost Zn single-atom anchored on curved N-doped carbon nanofibers (Zn SAs/N-C) by a facile noncovalent self-assembly approach. At a low overpotential of only 330 mV, the Zn SAs/N-C exhibited simultaneously both a high current density up to 121.5 mA cm^{-2} and a CO FE of 94.7%, superior to the previous reports. Experiments and DFT calculations revealed that the Zn atoms in Zn-N_4 acted as the active sites, while adjacent pyridine-N coupled with Zn-N_4 could synergistically decrease the free energy barrier for intermediate *COOH formation. Importantly, the curvature of catalyst induced Zn 3d electrons that were bound to the Zn-N bonds returned to Zn atom, thereby leading to an increase in electron density of Zn and facilitating CO_2 electroreduction to CO.

DOI: 10.1002/cctc.202001667

Table of Contents

Experimental Procedures

Chemicals and materials. Aniline (C_6H_7N) was purchased from Aladdin Reagent Co., Ltd., purified by vacuum distillation and kept under N_2 in a refrigerator prior to use. Ammonium persulfate ($(NH_4)_2S_2O_8$), zinc chloride ($ZnCl_2$), phosphate (H_3PO_4), potassium bicarbonate ($KHCO_3$) and hydrochloric acid (HCl) were purchased from Beijing Chemical Factory; Carbon nano tubes (CNTs) and graphene were purchased from XFNANO, INC; 4,4'-Bipyridine ($C_{10}H_8N_2$) from Innochem, and Nafion solution (5 wt%) from Alfa Aesar, both were used as received.

Preparation of polyaniline (PANI). 0.456 mL of Aniline was dispersed ultrasonically in 200 mL 1 M HCl aqueous solution at room temperature for 10 min to obtain a homogenous emulsion. 1.414 g of $(NH_4)_2S_2O_8$ that was dissolved in HCl (1 M, 20 mL) solution was added into the emulsion mentioned above and then stirred at 0 °C for 24 hours. After the completion of reaction, the as-obtained polyaniline (PANI) was centrifuged and washed with ethanol three times and dried in vacuum at 70 °C for overnight.

Preparation of catalysts. In a typical procedure, the powder of PANI (250 mg) was dispersed in ethanol (50 mL) under ultrasound for 30 min at room temperature. 87.3 mg of $ZnCl_2$ was added into PANI dispersion under stirring for 30 min to form homogeneous dispersion. And then, 50 mg of 4,4'-bipyridine that dissolved in ethanol (20 mL) was injected slowly into the mixed dispersion under vigorous stirring for 3 hours, followed by centrifugation and drying in vacuum at 70 °C for overnight to obtain black powder. After that, the black powder was transferred into a tubular furnace, where it was heated at 350 °C with a heating rate of 1 °C/min and held at this temperature for 2 h, and then it was heated to 1000 °C with a heating rate of 1 °C /min and held at 1000 °C for 1 hours under N_2 atmosphere with flow rate of 50 mL/min, followed by slow cooling to room temperature. The as-fabricated Zn SAs anchored on N-doped carbon nanofiber catalyst were denoted as Zn SAs/N-C. For comparisons, Zn SAs on N-doped carbon (Zn-N-C) and N-doped carbon nanofiber (N-C) were fabricated by direct pyrolysis of Zn (II) coordinated with 4,4′ -bipyridine and PANI nanofibers under the same conditions. Furthermore, Zn SAs on CNTs and graphene catalysts were respectively prepared under the same preparation conditions as for Zn SAs/N-C, except for different substrates, which were denoted as Zn SAs/CNTs and Zn SAs/G.

Catalyst characterization. X-ray diffraction (XRD) measurements were performed using a Rigaku X-ray powder diffractometer with Cu Kα X-ray source (λ=1.5418 Å). The morphologies were observed by a scanning electron microscope (SEM, JSM-6700F, 5 kV) and a transmission electron microscope (TEM, JEOL JEM-2100F, 200 kV). The actual loading of Zn in the sample was measured by ICP-MS (Agilent-7800). Raman spectroscopy was conducted on a LabRam HR Evolution with a 532 nm excitation laser. X-ray photoelectron spectroscopy (XPS) was carried out on Kratos AXIS SUPRA. N_2 adsorption/desorption was measured using a Quantachrome Autosorb iQ2 system at 77 K, and specific surface areas of the catalysts were measured by the Brunauer-Emmett-Teller (BET) equation. HAADF-STEM images were obtained on a JEOL LEM 2200FS/TEM, equipped with a CEOS probe corrector. X-ray absorption near edge structure (XANES) and extend X-ray absorption fine structure (EXAFS) were investigated on the 5-BMD beamline at the Advanced Photon Source (APS), and were provided with technical support by Ceshigo Research Service, Agency for XAS. The radiation was monochromatized by a Si (111) double-crystal monochromator. XANES and EXAFS data reduction and analysis were processed using Athena software.

Electrochemical measurements. The electrochemical measurements were carried out in a custom-designed two-compartment three electrode electrochemical cell using a CHI 750E electrochemical workstation (CH Instruments, Chenhua Co., Shanghai, China). The two compartments are separated by the anion exchange to prevent the CO_2 reduction products from being re-oxidized, and each compartment contains 30 mL electrolyte (0.5 M $KHCO_3$). The Zn SAs/N-C, Zn-N-C and N-C were used as working electrodes, Ag/AgCl electrode and Pt sheet were used as a reference electrode, and a counter electrode, respectively. In a typical prepared procedure of the working electrode, 200 μL of the homogeneous ink, which was prepared by dispersing 3 mg sample and 50 μL Nafion solution (5 wt%) in 350 μL ethanol solution, was loaded onto one side of a carbon paper electrode with 1×1 cm^2. The potentials were recorded versus RHE scale using the following conversion, according to the Eq. S1.

$$E\ (vs\ RHE) = E\ (vs\ Ag/AgCl) + 0.197\ V + 0.0591 \times pH \qquad (Eq.\ S1)$$

The current density was obtained by normalizing current with the catalytic geometrical surface area. Linear sweep voltammetry (LSV) curve was performed with the scan rate of 10 mV s^{-1} over a potential rang of 0.40 to -1.20 V (vs RHE) in 0.5 M $KHCO_3$. A pure CO_2 gas (99.99%) was bubbled into the electrolyte for 30 min to produce a saturated solution, prior to each experiment. The onset potentials for HER and electrochemical CO_2 reduction were determined from LSVs in N_2-saturated and CO_2-saturated electrolyte, respectively. The electrochemical CO_2 reduction process was conducted at the room temperature.

Gas-phase products were analyzed using a gas chromatograph (GC, SHIMADZY, GC-2014), which is equipped with a molecular sieve 13X and Q-bond PLOT columns. Ultra-high purity nitrogen (99.999%) was used as the carried gas for CO and H_2 detection. During electrolysis, CO_2 was continuously purged into electrochemical cell at a flow rate of 20 mL min^{-1} and at a pressure of 1 atm. The Faradaic efficiency (FE) of CO production was calculated as below:[1]

$$FE\% = \frac{2Fv_iGp_0}{RTj_{total}} \qquad (Eq.\ S2)$$

where v_i is the volume concentration of CO in the exhaust gas from the electrochemical cell (GC data), p_0 = 1.01 bar and T = 298.15 K, gas flow rate (G) measured by a D07 rotor meter at the exit of the electrochemical cell (mL min^{-1}), j_{total} is the steady-state current, F = 96485 C mol^{-1}, R = 8.314 J mol^{-1} K^{-1}. The partial current density (j_{CO}) of CO production was calculated as below:

$$j_{CO} = FE \times j_{total} \times (\text{electrode area})^{-1} \qquad (Eq.\ S3)$$

where electrode area is 1×1 cm^2.

Flow-type measurement was performed in a home-designed flow-type cell reactor. It consisted of catalyst-loaded carbon paper (~4 mg cm^{-2}) as the cathode, a piece of anion exchange membrane as the separator, and a Pt sheet as the anode. The Ag/AgCl reference electrode with a diameter of 3.8 mm was located inside the cathode compartment. During the measurement, CO_2 gas was directly fed to the cathode at a rate of 20 mL min^{-1} and at a pressure of 1 atm. The catholyte was 1 M $KHCO_3$. It was forced to continuously circulate through the cathode compartment at a rate of 50 mL min^{-1}.

The TOF for CO production from the CO_2 electro-reduction was calculated as follow:[1]

$$\mathrm{TOF}\ (\mathrm{h}^{-1}) = \frac{i_{CO}/(\beta F)}{m_{cat} \times \omega / M_{Zn}} \times 3600 \qquad \text{(Eq. S4)}$$

where i_{CO} is partial current (A) for CO product, β is the number of electron transferred for product formation, which is 2 for CO, F is Faradaic constant, 96485 C mol^{-1}, m_{cat} is catalyst mass in the electrode, g, ω is Zn loading in the catalyst (obtained from ICP analysis, ω = 0.13%), M_{Zn} is atomic mass of Zn, 65.38 g mol^{-1}.

DFT calculations. The density functional theory (DFT) calculation was carried out by using Vienna Ab-initio Simulation Package (VASP) along with the exchange-correlation functional of Perdew-Burke-Ernzerhof (PBE) generalized gradient approximation (GGA). The plane wave energy cutoff was set as 400 eV. The Fermi scheme was employed for electron occupancy with an energy smearing of 0.1 eV. The first Brillouin zone was sampled in the Monkhorst-Pack grid. The 3×3×1 k-point mesh was employed in the calculation. The energy (converged to 1.0 $\times 10^{-6}$ eV/atom) and force (converged to 0.01 eV/Å) were set as the convergence criterions for geometry optimization. The spin polarization was considered in all calculations. Both N atoms and Zn-N_4 sites were doped in graphene without and with curvature. For N atoms, three different N types, including pyridine-N, pyrrole-N and graphite-N species were considered. Besides, the possible coupled models of N species and Zn-N_4 were designed. In the structural optimization calculations, all of these atoms were allowed to relax. A vacuum layer as large as 15 Å was used along the c direction normal to avoid periodic interactions. The free energy changes of $CO_2 \rightarrow CO$ were investigated on possible active sites of N and Zn atoms, respectively. The free energy change (ΔG) of elementary reaction was defined as follows:

$$\Delta G = \Delta E_{DFT} + \Delta E_{ZPE} - T\Delta S \qquad \text{(Eq. S5)}$$

where ΔE_{DFT} is the reaction energy of elementary reaction obtained by DFT calculation, i.e. the energy difference between the final and initial states, ΔE_{ZPE} is the difference in zero-point energy between the final and initial states, while $T\Delta S$ is the entropy change of the elementary reaction.

The structural parameters of DFT model was shown as follows:

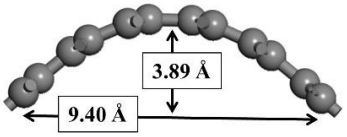

R=4.78 Å; K=0.209 $Å^{-1}$

Supplementary Figures and Tables

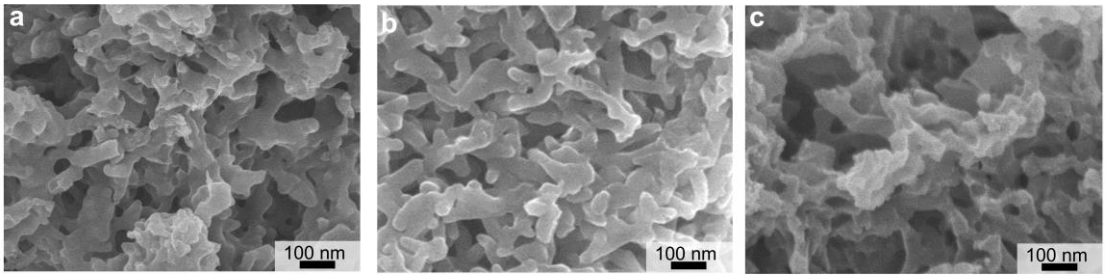

Figure S1. The optimization of the pyrolysis temperature for the preparation of Zn SAs/N-C catalysts. SEM images of Zn SAs/N-C catalysts prepared at 900 °C (a), 1000 °C (b) and 1100 °C (c).

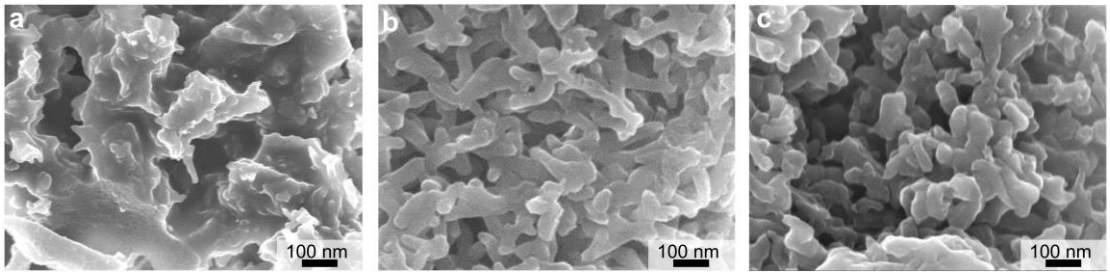

Figure S2. The optimization of Zn SAs/N-C catalyst synthesis by varying the mass ratio of 4,4'-Bipyridine/PANI. SEM images of Zn SAs/N-C catalysts prepared by using the mass ratios of 1:1 (a), 1:5 (b) and 1:10 (c).

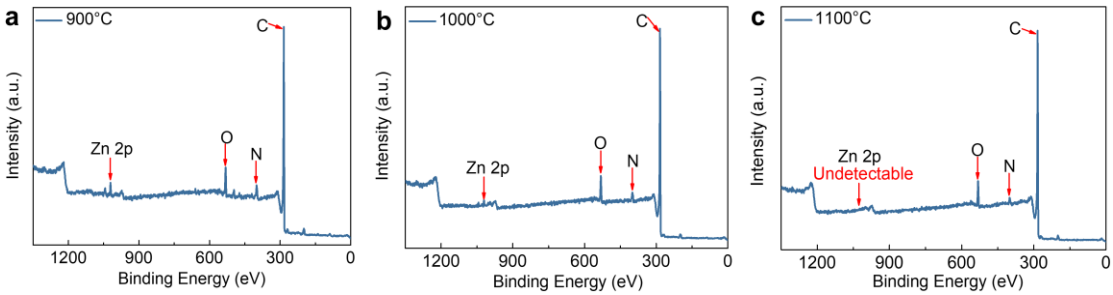

Figure S3. XPS spectra for the survey scan of Zn SAs/N-C catalysts prepared at different pyrolysis temperatures of (a) 900 °C, (b) 1000 °C and (c) 1100 °C.

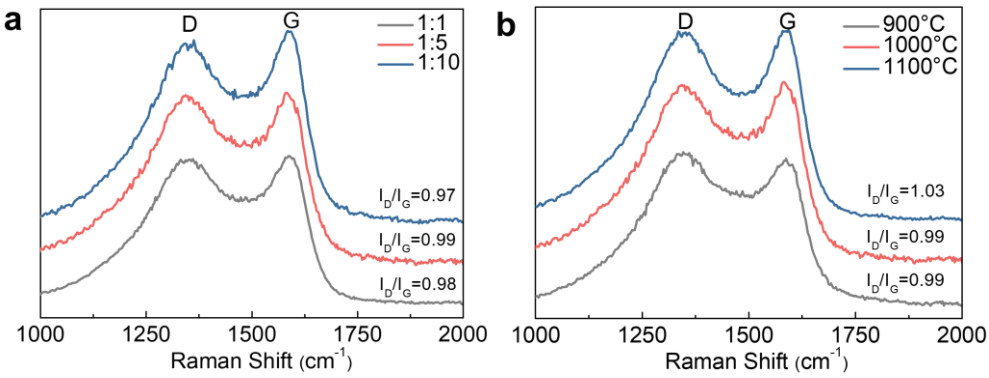

Figure S4. Raman spectra of Zn SAs/N-C catalysts prepared at (a) different mass ratios and (b) different pyrolysis temperatures.

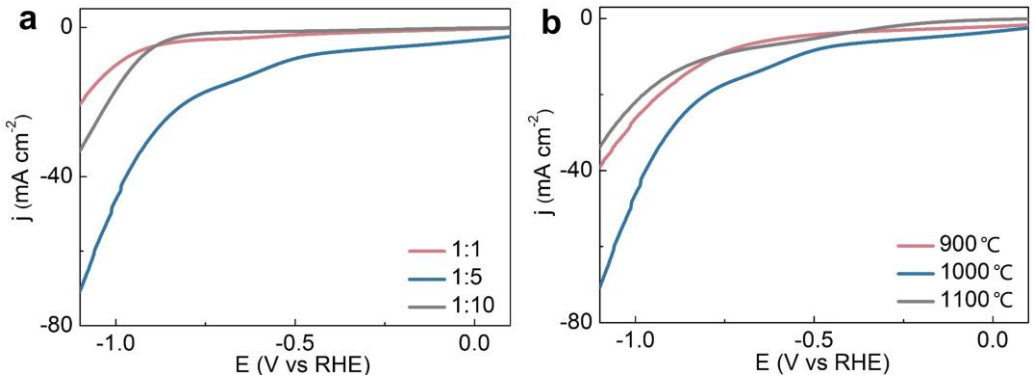

Figure S5. LSV curves of Zn SAs/N-C catalysts prepared at (a) different mass ratios and (b) different pyrolysis temperatures.

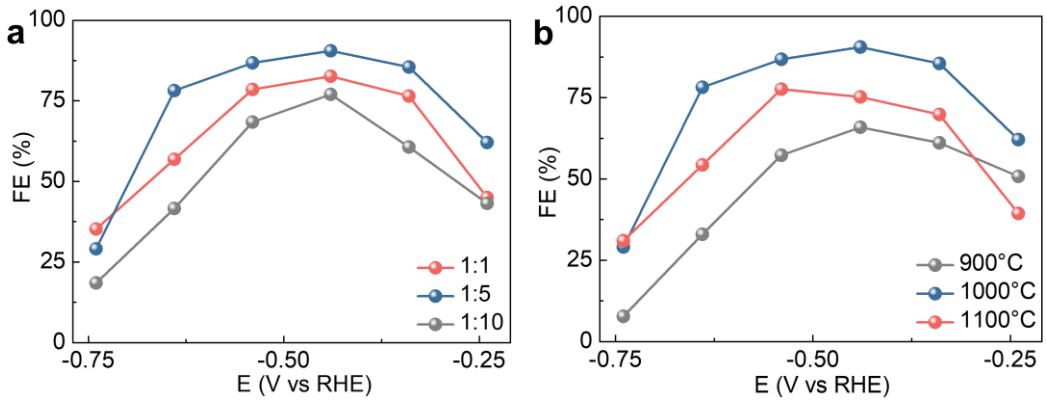

Figure S6. Faradaic efficiencies (FEs) of electroreduction of CO_2 to CO at different applied potentials on (a) Zn SAs/N-C catalysts prepared at different mass ratios and (b) Zn SAs/N-C catalysts prepared at different pyrolysis temperatures.

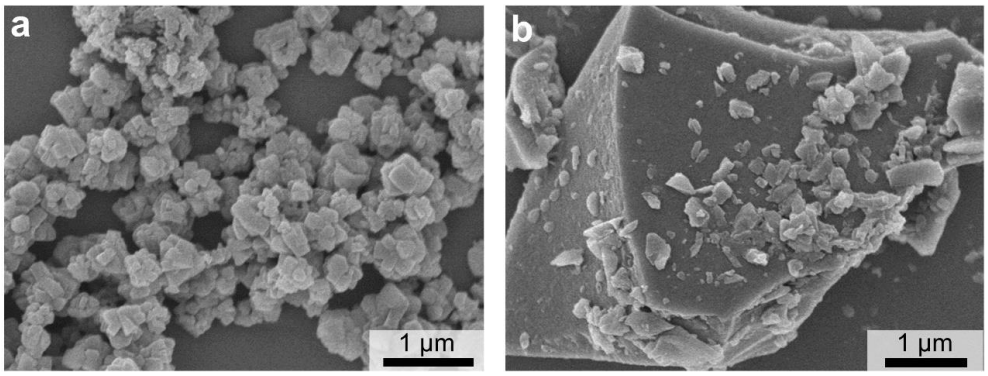

Figure S7. Characterizations of Zn-N-C precursor and as-prepared Zn-N-C catalyst. (a) SEM image of Zn-N-C precursor. (b) SEM image of Zn-N-C catalyst.

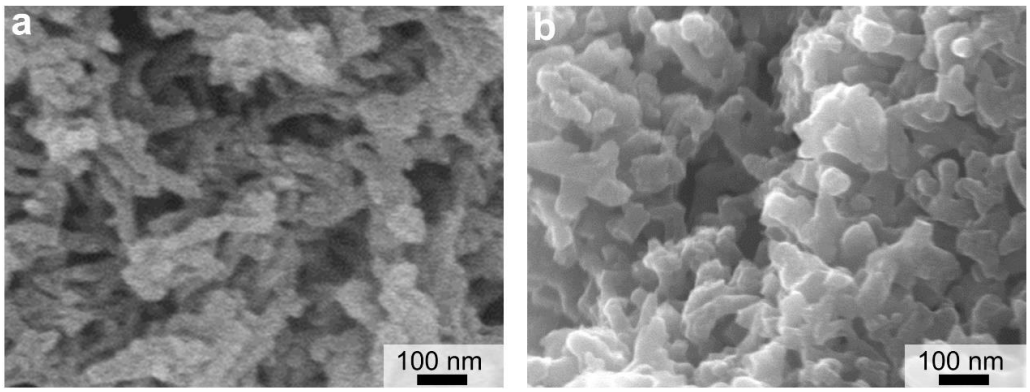

Figure S8. Characterizations of PANI and as-prepared N-C catalyst. (a) SEM image of PANI. (b) SEM image of N-C catalyst.

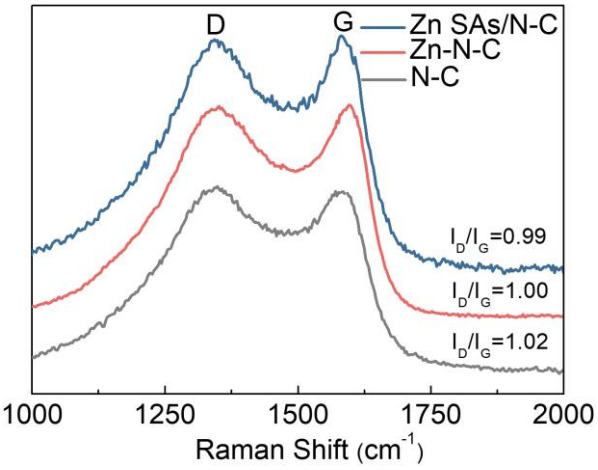

Figure S9. Raman spectra for Zn SAs/N-C, Zn-N-C, and N-C catalysts.

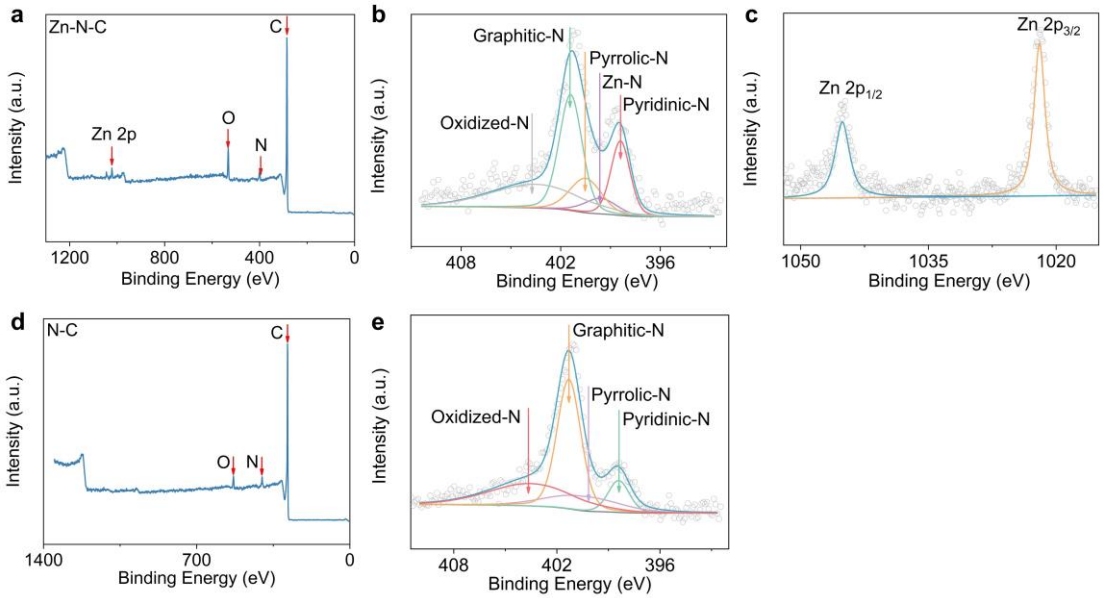

Figure S10. (a) XPS survey spectrum of Zn-N-C. (b) High-resolution N 1s XPS spectrum of Zn-N-C. (c) High-resolution Zn 2p XPS spectrum of Zn-N-C. (d) XPS survey spectrum for the scan of N-C. (e) High-resolution N 1s XPS spectrum of N-C.

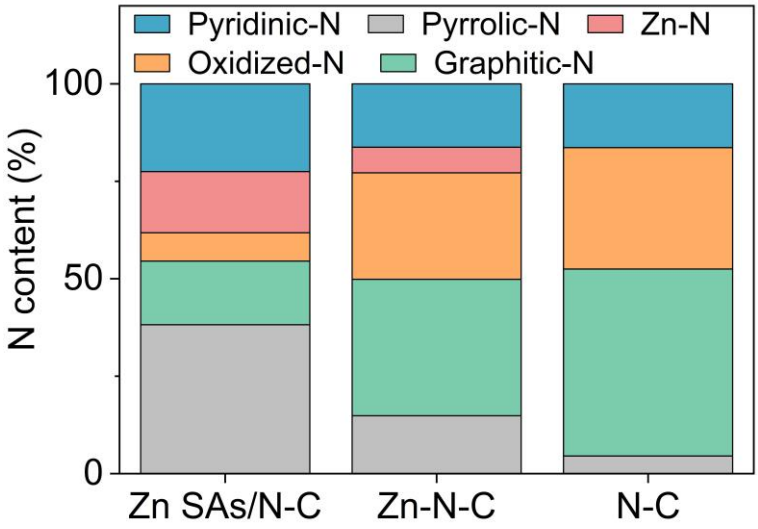

Figure S11. N content from High-resolution N 1s spectra of Zn SAs, Zn-N-C and N-C.

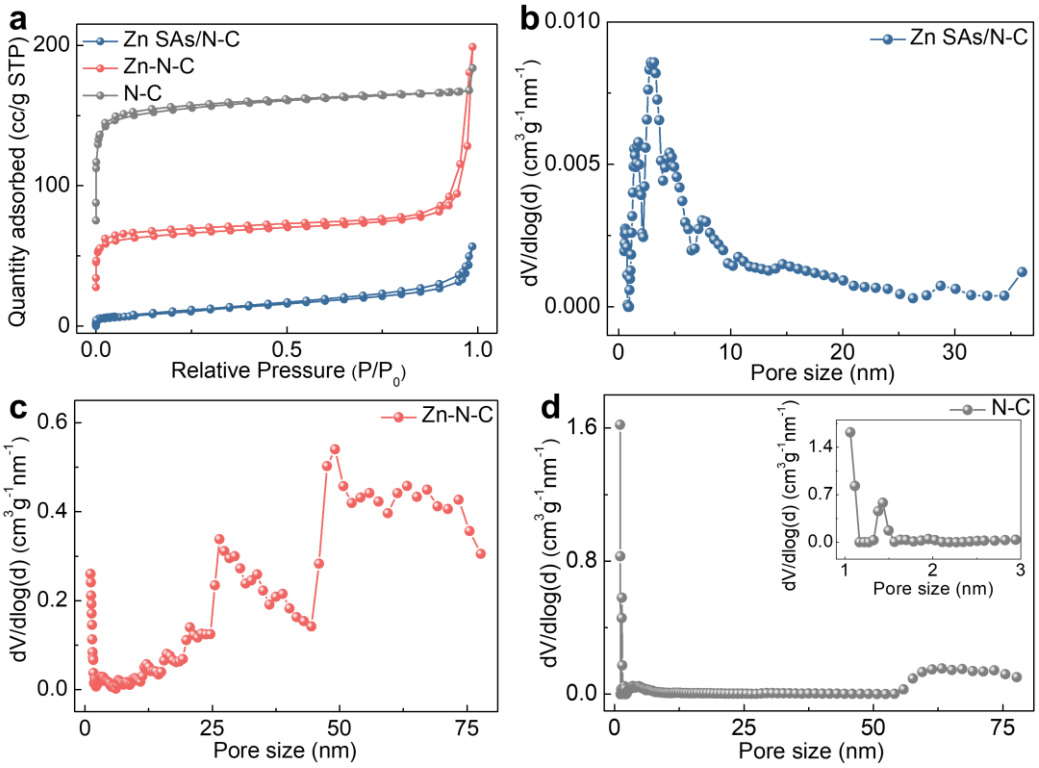

Figure S12. (a) N_2 adsorption and desorption isotherms obtained from Zn SAs/N-C, Zn-N-C, and N-C catalysts. (b-d) Pore size distributions of Zn SAs/N-C (b), Zn-N-C (c), and N-C (d).

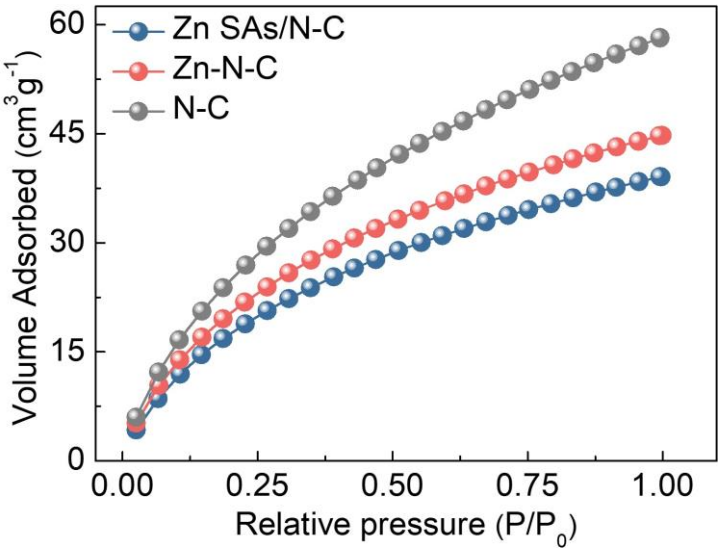

Figure S13. CO_2 adsorption isotherms collected from Zn SAs/N-C, Zn-N-C, and N-C catalysts.

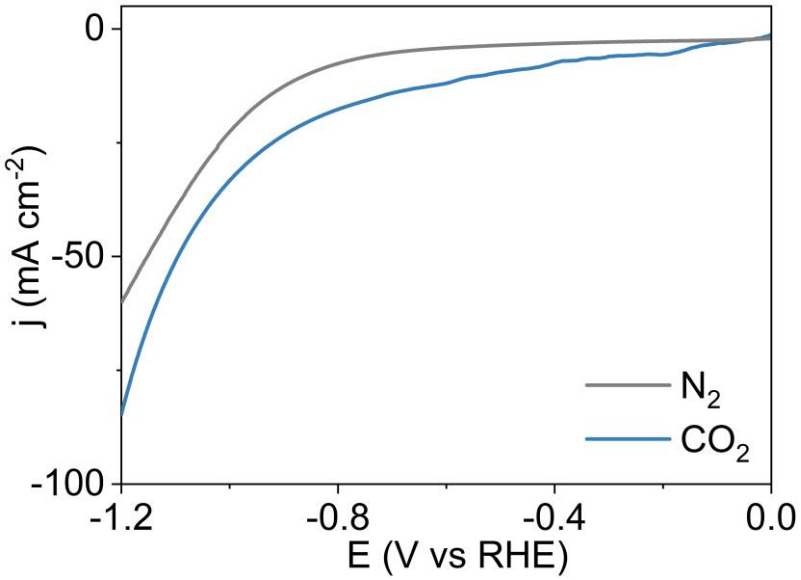

Figure S14. LSV curves of Zn SAs/N-C obtained in N_2- and CO_2-saturated 0.5 M $KHCO_3$ solutions, respectively.

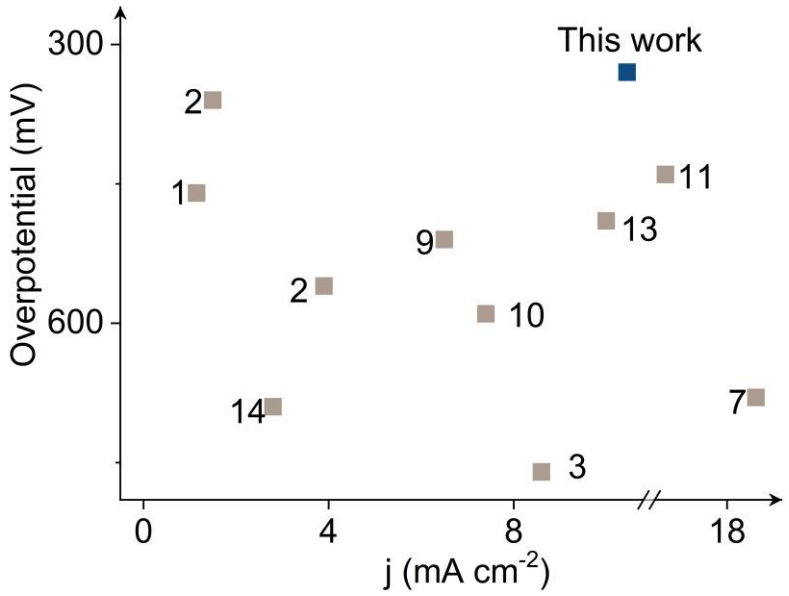

Figure S15. Comparison of our results with previous data in terms of current densities and overpotentials for CO_2RR in H-type cell. Note that overpotential of Zn SAs/N-C is smallest among the reported literatures (references in Table S2).

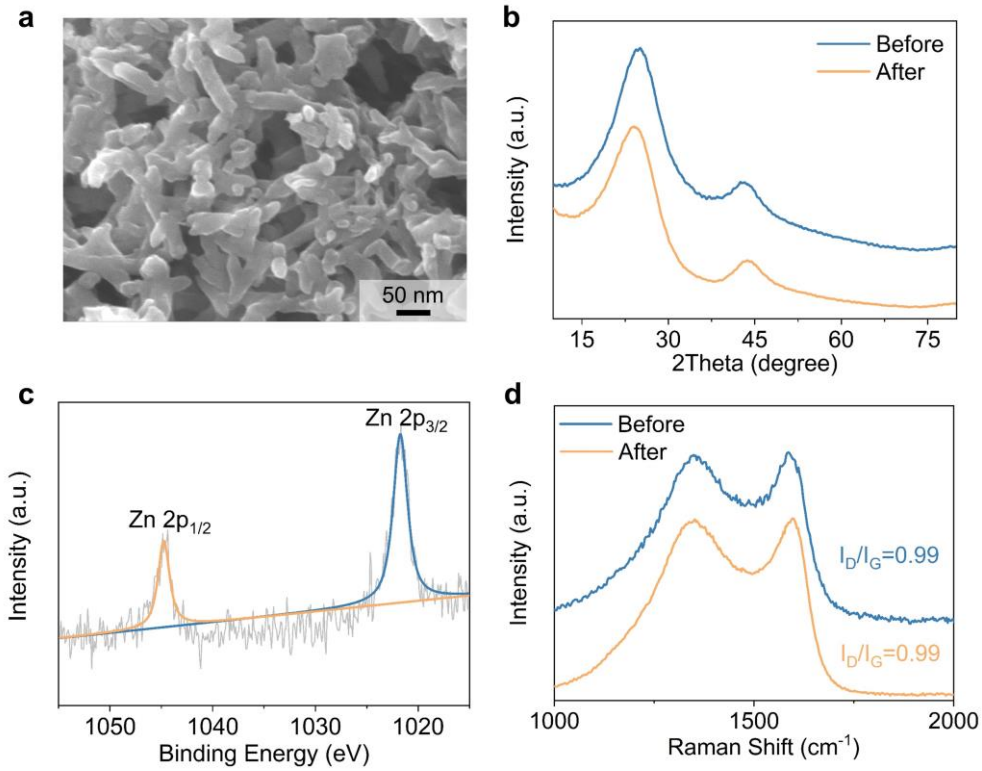

Figure S16. Zn SAs/N-C after electroreduction CO_2. (a) SEM image. (b) XRD patterns. (c) High-resolution Zn 2p spectra. (d) Raman spectra.

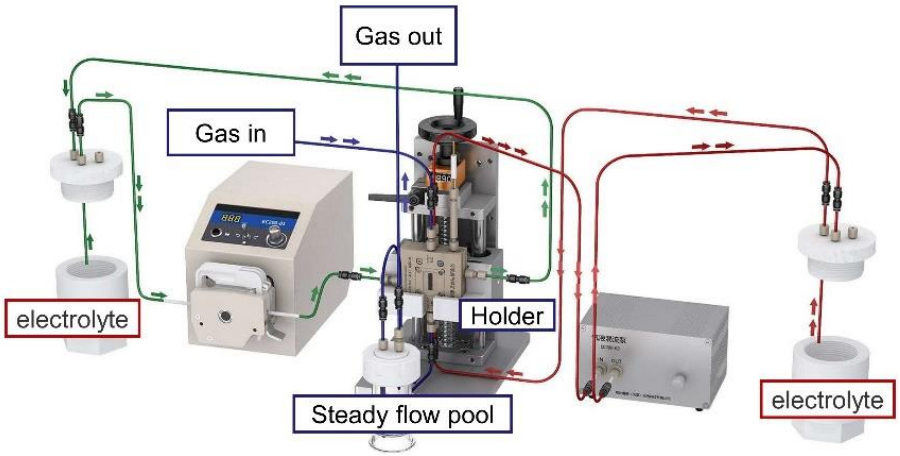

Figure S17. Schematic illustration of the Flow-type cell.

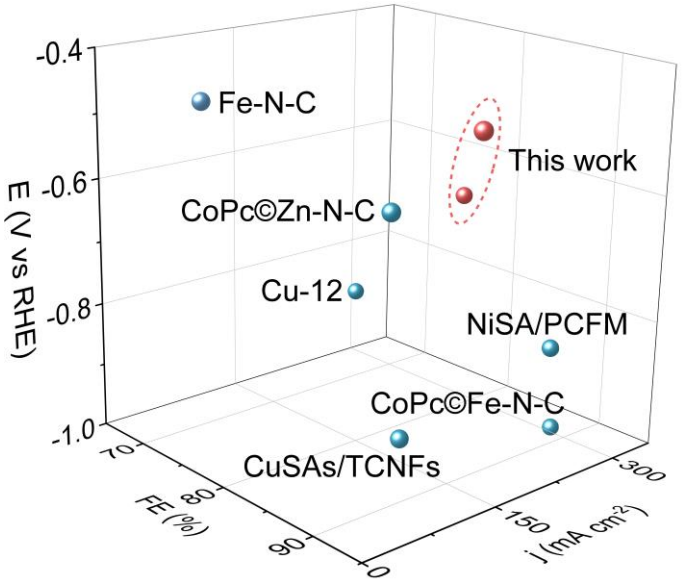

Figure S18. Comparison of our results with previous data in terms of FEs, current densities and overpotentials for CO_2RR in flow-type cell (references in Table S3).

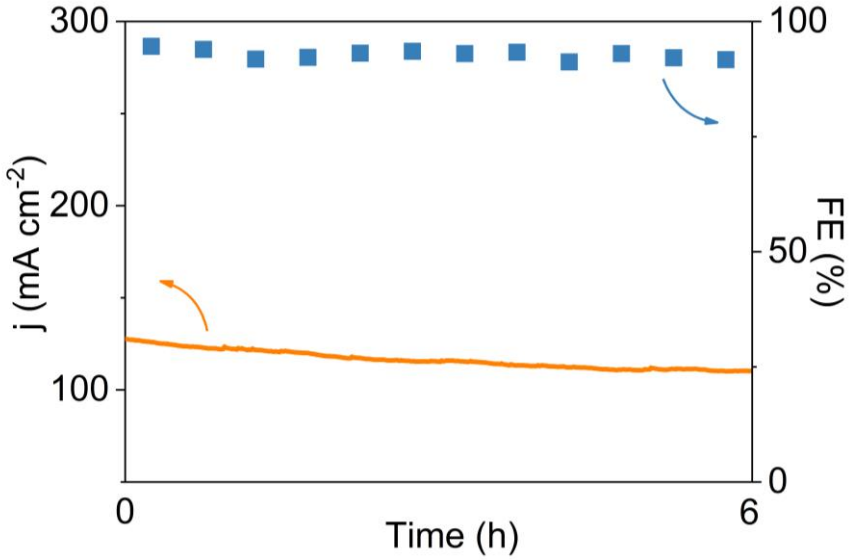

Figure S19. Chronoamperometry curve and FE of CO production on Zn SAs/N-C at -0.44 V (vs RHE) for 6 hours.

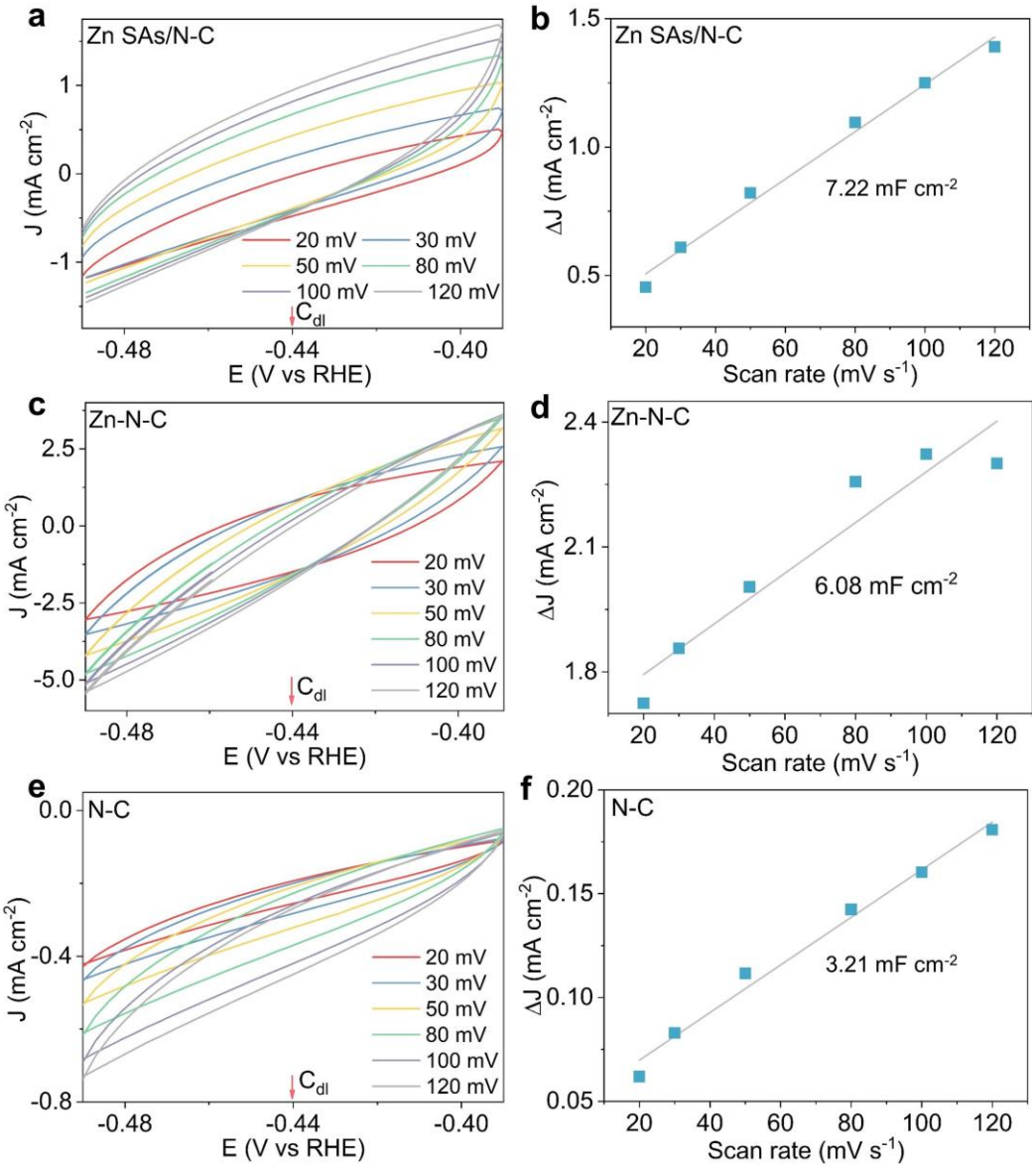

Figure S20. (a, c, e) Electrochemical double layer capacitances (EDLCs) for Zn SAs/N-C, Zn-N-C and N-C in N_2-bubbled 0.5 M $KHCO_3$. (b, d, f) Electrochemical active surface areas (ECSAs) estimated from the EDLCs of Zn SAs/N-C, Zn-N-C and N-C.

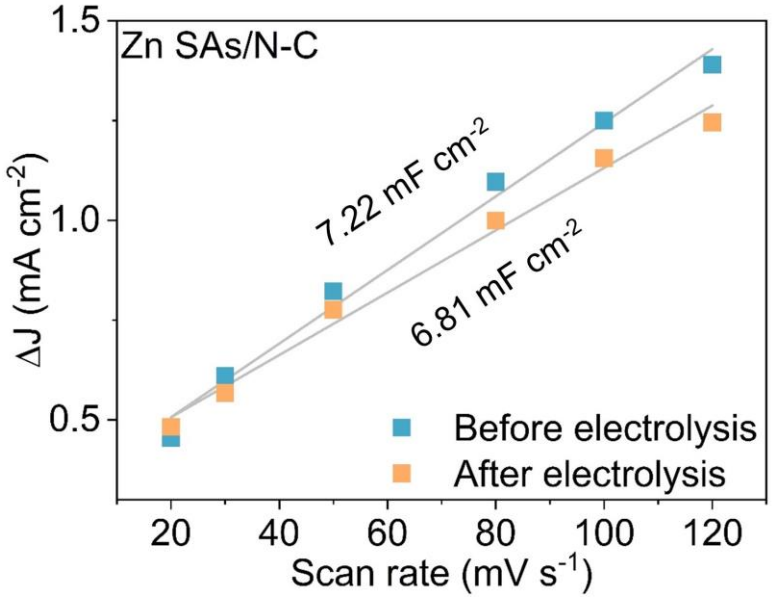

Figure S21. ECSA of Zn SAs/N-C as a function of scan rate before and after electrolysis.

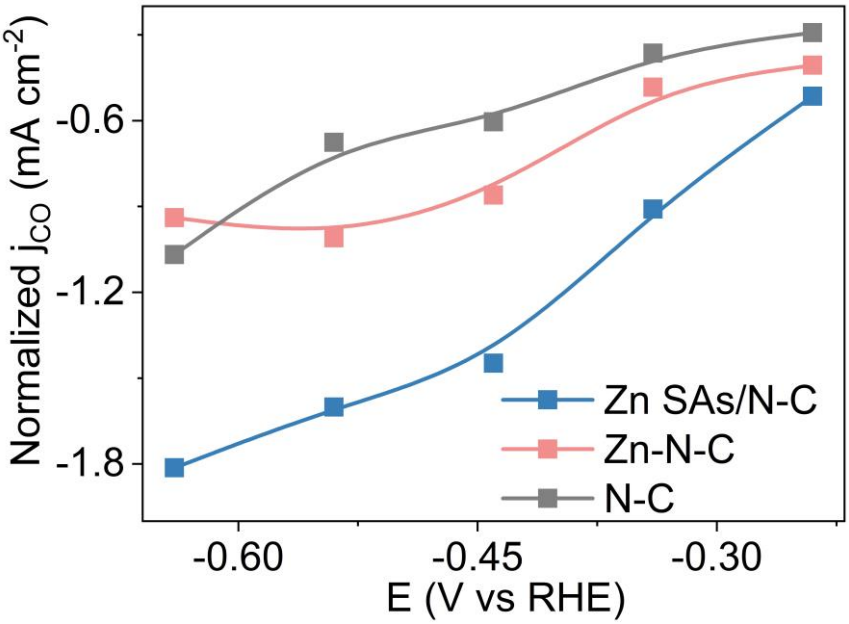

Figure S22. Current densities of Zn SAs/N-C, Zn-N-C and N-C normalized by ECSA.

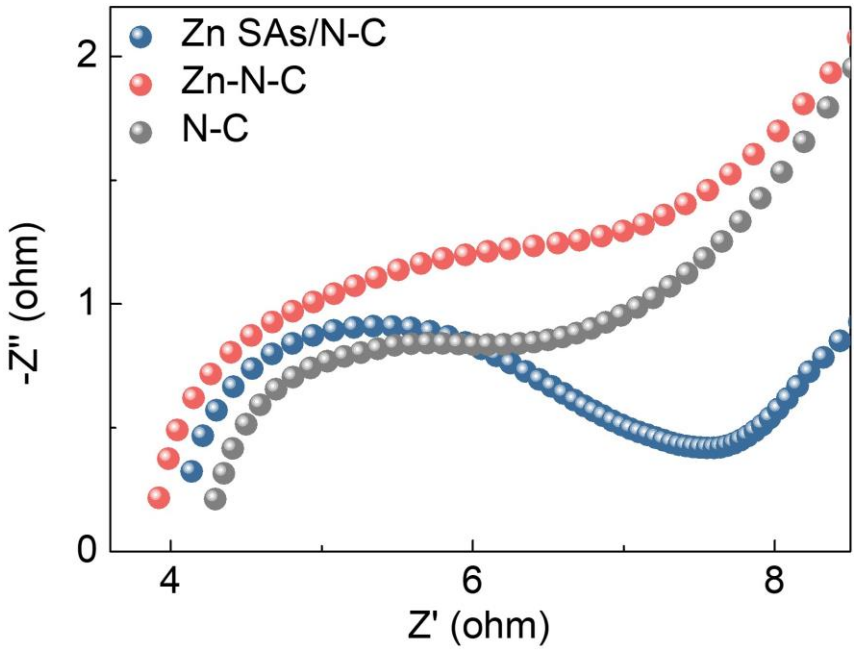

Figure S23. Nyquist plots of Zn SAs/N-C, Zn-N-C, and N-C electrocatalysts.

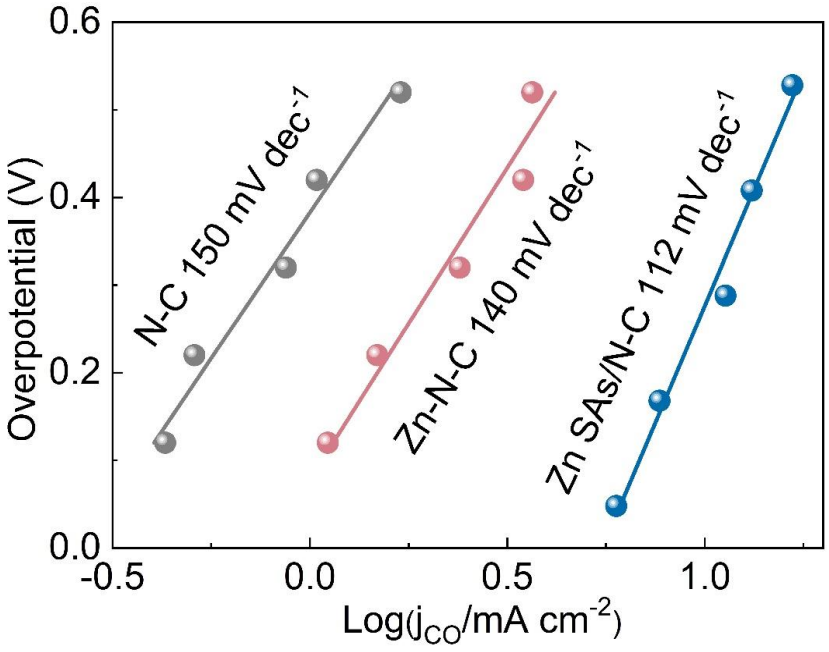

Figure S24. Tafel plots of the partial current density of CO formation for Zn SAs/N-C, Zn-N-C, and N-C at different applied potentials.

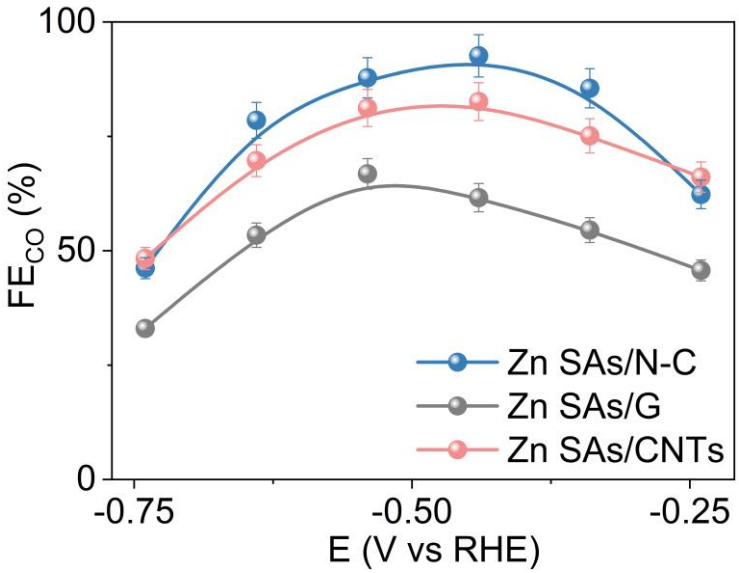

Figure S25. FEs of CO formation on Zn SAs/N-C, Zn SAs/G and Zn SAs/CNTs.

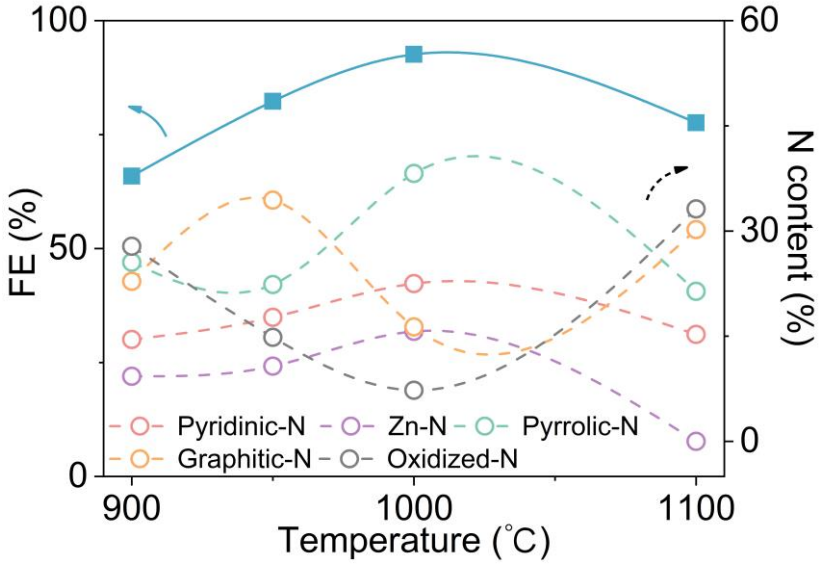

Figure S26. The relationship between the maximum CO FEs, contents of N species in Zn SAs/N-C and the pyrolysis temperature.

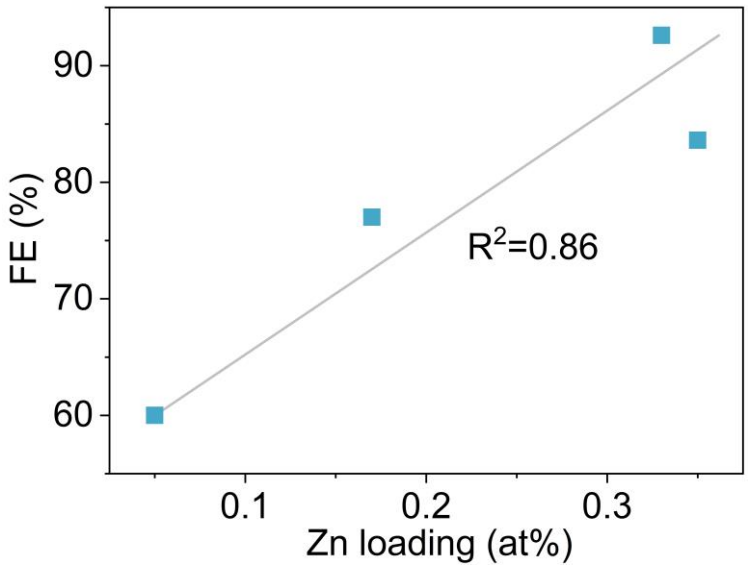

Figure S27. The correlation between CO FEs and Zn loadings on Zn SAs/N-C catalysts.

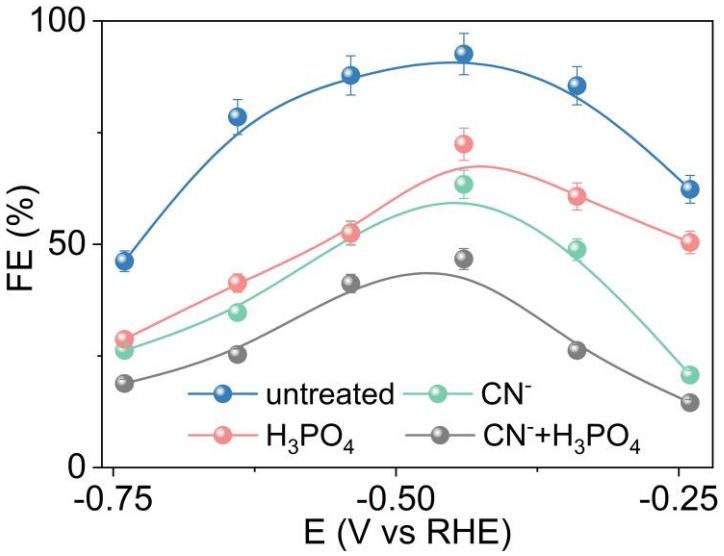

Figure S28. FEs of CO formation on Zn SAs/N-C, before and after being poisoned by CN^-, H_3PO_4 and $CN^-+H_3PO_4$.

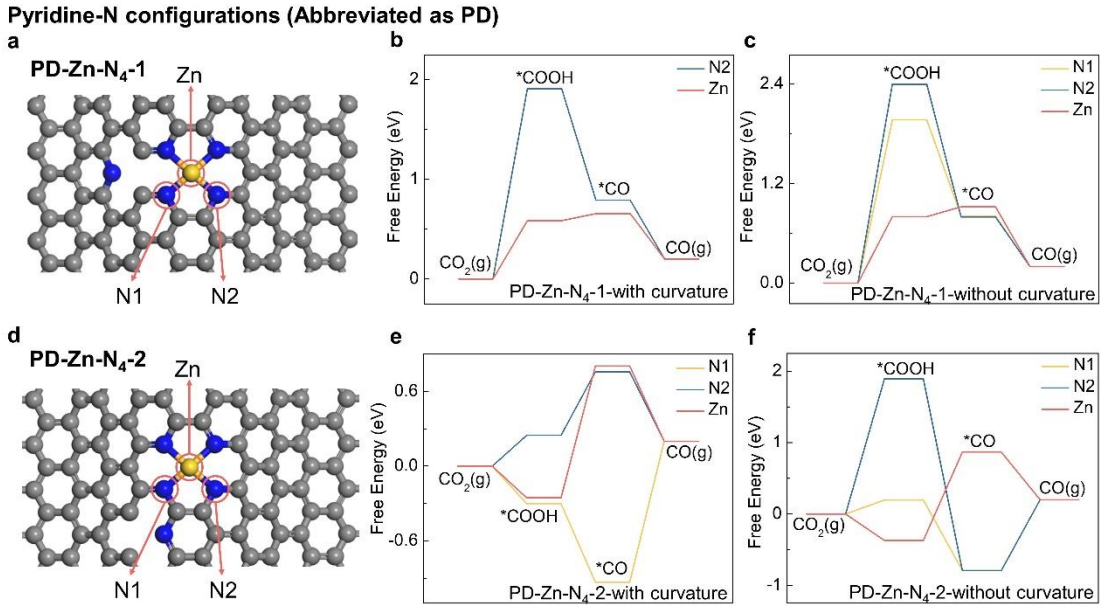

Figure S29. The models were denoted as PD-Zn-N_4-X, where X=1 and 2, the numbers represent the different relative positions of Zn-N_4 and N. The yellow and blue balls correspond to the Zn atom and N atoms, respectively. (a) Top view of the optimized structure for PD-Zn-N_4-1. (b-c) Free energy diagram for the conversion of CO_2 to CO on differently coupled sites at U=0 V versus RHE on PD-Zn-N_4-1-with curvature and PD-Zn-N_4-1-without curvature, respectively. (d) Top view of the optimized structure for PD-Zn-N_4-2. (e-f) Free energy diagram for the conversion of CO_2 to CO on differently coupled sites at U=0 V versus RHE on the PD-Zn-N_4-2-with curvature and PD-Zn-N_4-2-with curvature, respectively.

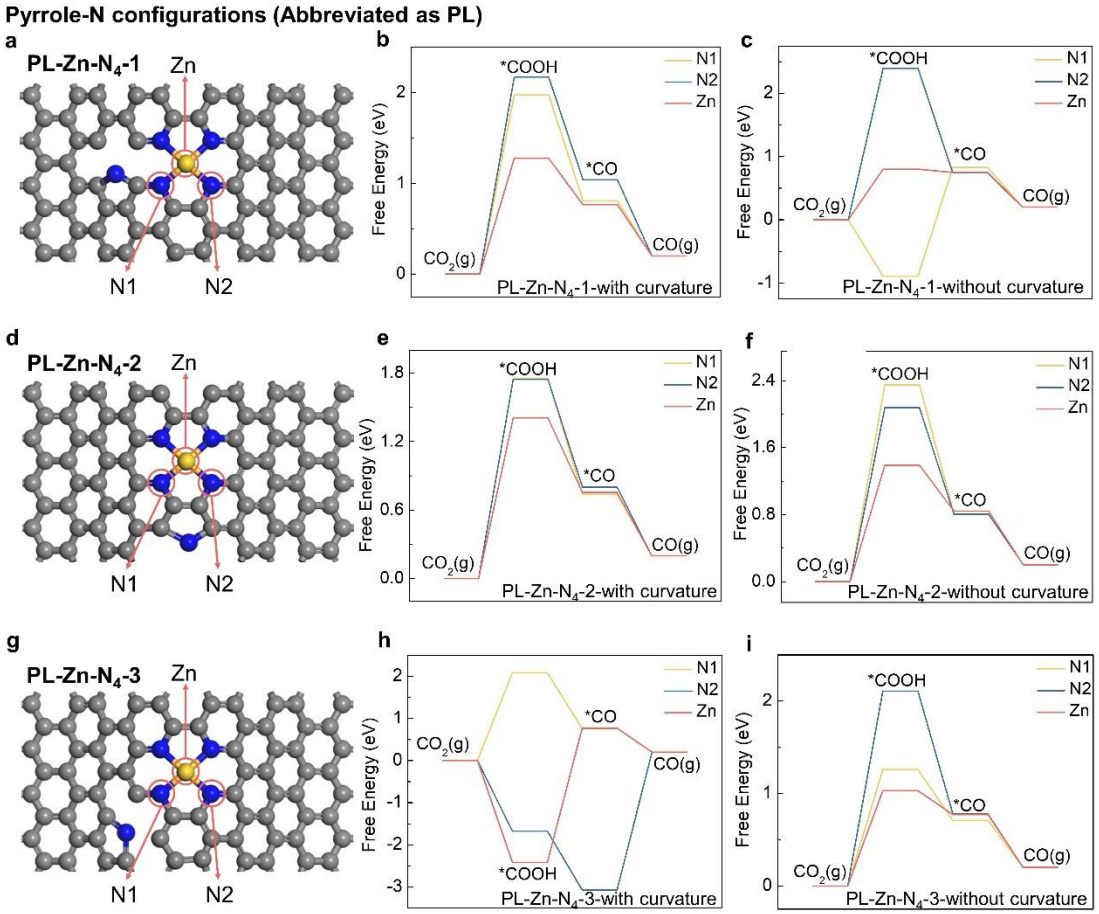

Figure S30. The models were denoted as PL-Zn-N_4-X, where X=1, 2 and 3, the numbers represent the different relative positions of Zn-N_4 and N. The yellow and blue balls correspond to the Zn atom and N atoms, respectively. (a) Top view of the optimized structure for PL-Zn-N_4-1. (b-c) Free energy diagram for the conversion of CO_2 to CO on differently coupled sites at U=0 V versus RHE on PL-Zn-N_4-1-with curvature and PL-Zn-N_4-1-without curvature, respectively. (d) Top view of the optimized structure for PL-Zn-N_4-2. (e-f) Free energy diagram for the conversion of CO_2 to CO on differently coupled sites at U=0 V versus RHE on PL-Zn-N_4-2-with curvature and PL-Zn-N_4-2-without curvature, respectively. (g) Top view of the optimized structure for PL-Zn-N_4-3. (h-i) Free energy diagram for the conversion of CO_2 to CO on differently coupled sites at U=0 V versus RHE on PL-Zn-N_4-3-with curvature and PL-Zn-N_4-3-without curvature, respectively.

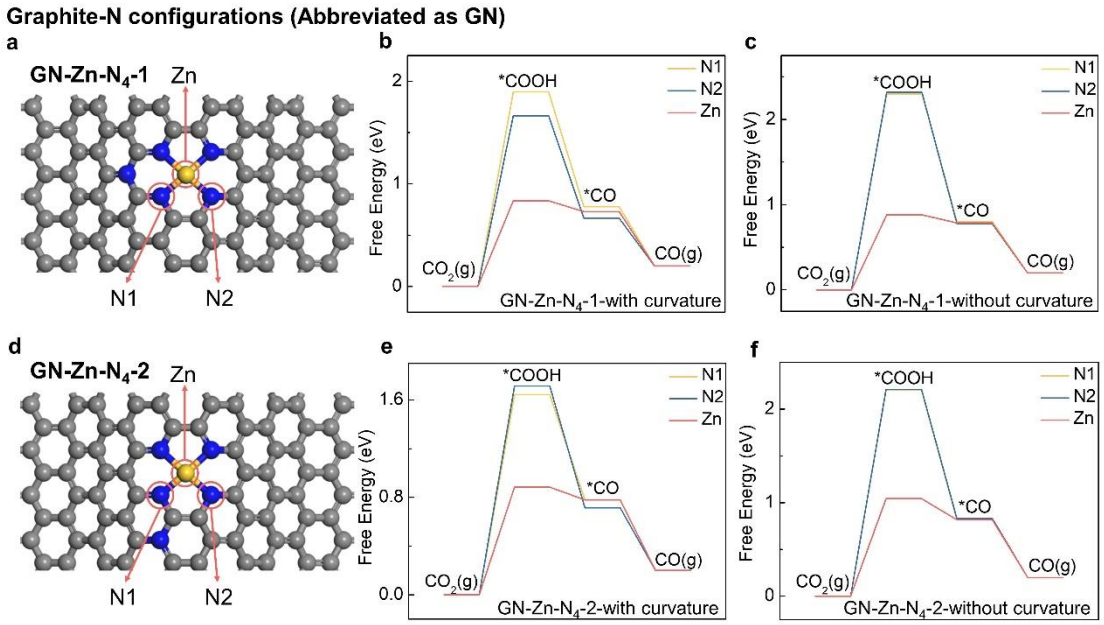

Figure S31. The models were denoted as GN-Zn-N_4-X, where X=1 and 2, the numbers represent the different relative positions of Zn-N_4 and N. The yellow and blue balls correspond to the Zn atom and N atoms, respectively. (a) Top view of the optimized structure for GN-Zn-N_4-1. (b-c) Free energy diagram for the conversion of CO_2 to CO on different coupled sites at U=0 V versus RHE on GN-Zn-N_4-1-with curvature and GN-Zn-N_4-1-without curvature, respectively. (d) Top view of the optimized structure for GN-Zn-N_4-2. (e-f) Free energy diagram for the conversion of CO_2 to CO on differently coupled sites at U=0 V versus RHE on GN-Zn-N_4-2-with curvature and GN-Zn-N_4-2-without curvature, respectively.

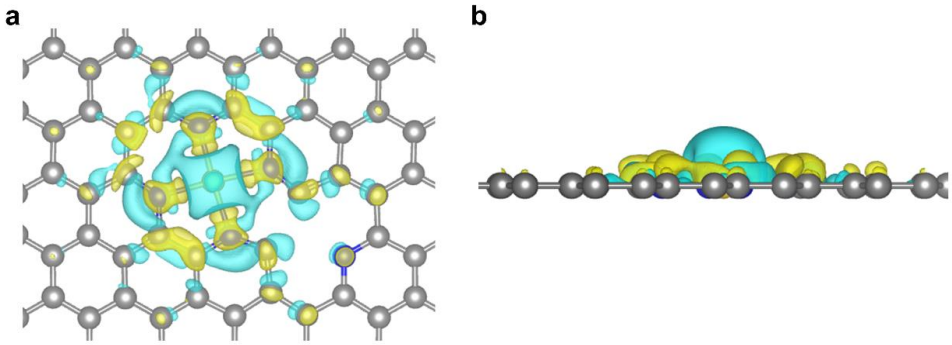

Figure S32. Differential charge density of PD-Zn-N_4-1-without curvature. The yellow and blue isosurfaces correspond to the increase in the number of electrons and the depletion zone, respectively.

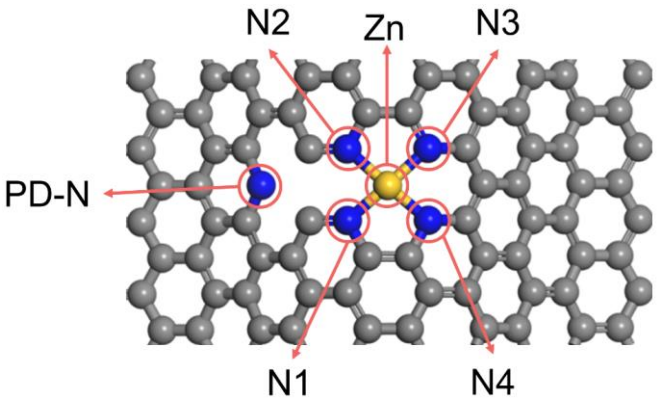

Figure S33. The labeling of sites of bader charge.

Table S1. EXAFS fitting parameters at the Zn K-edge for various samples（S_0^2=0.810）

Sample	Shell	N^a	R (Å)^b	σ^2 (Å^2)^c	ΔE_0 (eV)^d	R factor
Zn-N_4	Zn-N	3.5	1.98	0.0058	6.9	0.0010
Zn-N_2	Zn-N	2	2.14	0.0016	18.2	0.0820
Zn-N_6	Zn-N	6	2.14	0.0112	15.8	0.0146
Zn-C_4	Zn-C	4	2.07	0.0027	14.1	0.0197
Zn-C_6	Zn-C	6	2.06	0.0072	12.7	0.0033
Zn-O_4	Zn-O	4	2.10	0.0159	7.2	0.1190
Zn-O_6	Zn-O	6	2.10	0.0193	6.3	0.0730

[a]*N*: coordination numbers; [b]*R*: bond distance; [c]σ^2: Debye-Waller factor; [d] ΔE_0: the inner potential correction. *R* factor: goodness of fit. S_0^2 was set to 0.810, according to the experimental EXAFS fit of Zn foil reference by fixing CN as the known crystallographic value.

Table S2. Comparison of the activities of other reported SACs for CO_2RR (H-type cell).

Catalyst	Active site	Catholyte	Product	$FE_{product}$ (%)	Potent. (V vs RHE)	*j* (mA cm^{-2})	Ref.
Zn SAs/N-C	Pyridine N+Zn-N_4	0.5 M $KHCO_3$	CO	92.6	-0.44	10.45	This work
Fe-N-C coated NPS	Fe-N_x	0.5 M $KHCO_3$	CO	80	-0.57	1.15	[2]
Fe-N-C	Fe-N_x	0.5 M $KHCO_3$	CO	85	-0.47	1.5	[3]
Ni-NG	Ni- N_x	0.5 M $KHCO_3$	CO	93	-0.87	8.6	[4]
Ni-N-C	Ni- N_x	0.5 M $KHCO_3$	CO	93	-0.67	3.9	[3]
Co-N_2	Co-N_2	0.5 M $KHCO_3$	CO	95	-0.68	-	[5]
A-Ni-NSG	Ni-N_3S	0.5 M $KHCO_3$	CO/CH_4	97	-0.61	-	[6]
Fe-N-C	Fe-N_4/ Fe-N_{2+2}	0.1 M $KHCO_3$	CO	93	-0.58	-	[7]
Co-N_5	Co-N_5	0.2 M $NaHCO_3$	CO	99.3	-0.79	10.2	[8]
Ni_{SA}-N_x-C	Ni_{SA}-N_2-C	0.5 M $KHCO_3$	CO	98	-0.8	-	[9]
STPyP-Co	Co-N_4	0.5 M $KHCO_3$	CO	96	-0.62	6.5	[10]
Ni/Fe-N-C	Ni-Fe-N	0.5 M $KHCO_3$	CO	90	-0.7	7.4	[11]
Ni-N-MEGO	Ni-N_x	0.5 M $KHCO_3$	CO	92.1	-0.55	16.3	[12]
NiSA/PCFM	Ni-N_4	0.5 M $KHCO_3$	CO	96	-0.7	-	[13]
(Cl, N)-Mn/G	Mn-N_4-Cl	0.5 M $KHCO_3$	CO	97	-0.6	10	[14]
Nb_4N_5-NO/NC	Nb_4N_5	0.1 M $KHCO_3$	CO	91	-0.8	2.8	[15]

Table S3. Comparison of the activities of other reported catalysts for CO_2RR (Flow-type cell).

Catalyst	Catholyte	Product	$FE_{product}$ (%)	Potent. (V vs RHE)	*j* (mA cm^{-2})	Ref.
Zn SAs/N-C	1.0 M $KHCO_3$	CO	94.7	-0.44	121.5	This work
Zn SAs/N-C	1.0 M $KHCO_3$	CO	80.6	-0.64	271.8	This work
Ni-NG	0.5 M $KHCO_3$	CO	90%	2.78 (cell votage)	50.0	[4]
CuSAs/TCNFs	0.1 M $KHCO_3$	C_1	90%	-0.90	93.0	[16]
Fe-N-C	0.5 M KOH	CO	~75%	-0.45	24.6	[17]
CoPc©Zn-N-C	0.5 M KOH	CO	> 90%	-0.56	77.8	[17]
CoPc©Fe-N-C	0.5 M KOH	CO	> 90%	-0.84	275.6	[17]
CoPc	1 M KOH	CO	> 95%	~2.7 (cell votage)	150	[18]
Ni SACs	0.1 M $KHCO_3$	CO	99%	2.8 (cell votage)	83	[19]
NiSA/PCFM	0.5 M $KHCO_3$	CO	88%	-1.0	308.4	[13]
Cu-12	0.1 M $KHCO_3$	C_2H_4	72%	-0.83	232	[20]

Table S4. Free energy corrections for species (Pyridine-N (PD) with curvature).

Nitrogen	Site	Intermediate	E_{DFT} (eV)	E_{ZPE} (eV)	TΔS (eV)	G (eV)
PD-Zn-N_4-1-with curvature	N1	*COOH	-	-	-	-
		*CO	-	-	-	-
	N2	*COOH	-722.57	0.67	0.16	-722.06
		*CO	-712.11	0.15	0.33	-712.29
	Zn	*COOH	-723.74	0.60	0.26	-723.4
		*CO	-712.39	0.17	0.20	-712.42
PD-Zn-N_4-2-with curvature	N1	*COOH	-723.9	0.66	0.22	-723.46
		*CO	-713.03	0.16	0.33	-713.2
	N2	*COOH	-723.36	0.66	0.22	-722.92
		*CO	-711.29	0.15	0.37	-711.51
	Zn	*COOH	-723.76	0.6	0.26	-723.42
		*CO	-711.43	0.17	0.20	-711.46

Table S5. Free energy corrections for species (Pyrrole-N (PL) with curvature).

Nitrogen	Site	Intermediate	E_{DFT} (eV)	E_{ZPE} (eV)	TΔS (eV)	G (eV)
PL-Zn-N_4-1-with curvature	N1	*COOH	-722.78	0.67	0.16	-722.27
		*CO	-712.36	0.15	0.33	-712.54
	N2	*COOH	-722.58	0.67	0.16	-722.07
		*CO	-712.11	0.15	0.35	-712.31
	Zn	*COOH	-723.31	0.60	0.27	-722.98
		*CO	-712.56	0.17	0.20	-712.59
PL-Zn-N_4-2-with curvature	N1	*COOH	-724.82	0.66	0.22	-724.38
		*CO	-714.26	0.15	0.38	-714.49
	N2	*COOH	-724.82	0.66	0.22	-724.38
		*CO	-714.25	0.15	0.33	-714.43
	Zn	*COOH	-725.04	0.60	0.28	-724.72
		*CO	-714.44	0.17	0.21	-714.48
PL-Zn-N_4-3-with curvature	N1	*COOH	-720.17	0.66	0.21	-719.72
		*CO	-709.94	0.15	0.36	-710.15
	N2	*COOH	-723.94	0.66	0.20	-723.48
		*CO	-713.79	0.15	0.33	-713.97
	Zn	*COOH	-724.54	0.60	0.28	-724.22
		*CO	-710.09	0.17	0.21	-710.13

Table S6. Free energy corrections for species (Graphitic-N (GN) with curvature).

Nitrogen	Site	Intermediate	E_{DFT} (eV)	E_{ZPE} (eV)	TΔS (eV)	G (eV)
GN-Zn-N_4-1-with curvature	N1	*COOH	-735.94	0.66	0.20	-735.48
		*CO	-725.5	0.16	0.34	-725.68
	N2	*COOH	-736.17	0.66	0.20	-735.71
		*CO	-725.54	0.15	0.41	-725.8
	Zn	*COOH	-736.87	0.60	0.26	-736.53
		*CO	-725.69	0.17	0.21	-725.73
GN-Zn-N_4-2-with curvature	N1	*COOH	-736.24	0.66	0.20	-735.78
		*CO	-725.54	0.15	0.35	-725.74
	N2	*COOH	-736.17	0.66	0.20	-735.71
		*CO	-725.54	0.15	0.41	-725.8
	Zn	*COOH	-736.87	0.60	0.26	-736.53
		*CO	-725.7	0.17	0.21	-725.74

Table S7. Free energy corrections for species (Pyridine-N (PD) without curvature).

Nitrogen	Site	Intermediate	E_{DFT} (eV)	E_{ZPE} (eV)	TΔS (eV)	G (eV)
PD-Zn-N_4-1-without curvature	N1	*COOH	-652.26	0.62	0.17	-651.81
		*CO	-641.88	0.16	0.33	-642.05
	N2	*COOH	-651.84	0.66	0.19	-651.37
		*CO	-641.92	0.16	0.31	-642.07
	Zn	*COOH	-653.3	0.59	0.27	-652.98
		*CO	-641.88	0.16	0.23	-641.95
PD-Zn-N_4-2-without curvature	N1	*COOH	-652.71	0.68	0.17	-652.20
		*CO	-642.12	0.16	0.32	-642.28
	N2	*COOH	-650.98	0.66	0.18	-650.50
		*CO	-642.12	0.16	0.33	-642.29
	Zn	*COOH	-653.1	0.59	0.27	-652.78
		*CO	-640.55	0.16	0.25	-640.64

Table S8. Free energy corrections for species (Pyrrole-N (PL) without curvature).

Nitrogen	Site	Intermediate	E_{DFT} (eV)	E_{ZPE} (eV)	TΔS (eV)	G (eV)
PL-Zn-N_4-1-without curvature	N1	*COOH	-654.89	0.63	0.40	-654.66
		*CO	-641.88	0.15	0.31	-642.04
	N2	*COOH	-651.83	0.66	0.20	-651.37
		*CO	-642.07	0.16	0.22	-642.13
	Zn	*COOH	-653.30	0.60	0.27	-652.97
		*CO	-642.07	0.16	0.22	-642.13
PL-Zn-N_4-2-without curvature	N1	*COOH	-652.84	0.66	0.19	-652.37
		*CO	-642.84	0.15	0.33	-643.02
	N2	*COOH	-653.11	0.65	0.18	-652.64
		*CO	-642.83	0.16	0.34	-643.01
	Zn	*COOH	-653.65	0.59	0.27	-653.33
		*CO	-642.90	0.16	0.25	-642.99
PL-Zn-N_4-3-without curvature	N1	*COOH	-649.97	0.66	0.17	-649.48
		*CO	-638.94	0.15	0.35	-639.14
	N2	*COOH	-649.09	0.65	0.19	-648.63
		*CO	-638.89	0.16	0.33	-639.06
	Zn	*COOH	-650.02	0.59	0.28	-649.71
		*CO	-638.96	0.16	0.27	-639.07

Table S9. Free energy corrections for species (Graphitic-N (GN) without curvature).

Nitrogen	Site	Intermediate	E_{DFT} (eV)	E_{ZPE} (eV)	TΔS (eV)	G (eV)
GN-Zn-N_4-1-without curvature	N1	*COOH	-665.09	0.65	0.20	-664.64
		*CO	-655.06	0.15	0.34	-655.25
	N2	*COOH	-665.09	0.66	0.20	-664.63
		*CO	-655.09	0.15	0.34	-655.28
	Zn	*COOH	-666.38	0.59	0.27	-666.06
		*CO	-655.22	0.16	0.21	-655.27
GN-Zn-N_4-2-without curvature	N1	*COOH	-665.29	0.65	0.21	-664.85
		*CO	-655.16	0.16	0.33	-655.33
	N2	*COOH	-665.31	0.65	0.19	-664.85
		*CO	-655.17	0.16	0.32	-655.33
	Zn	*COOH	-666.33	0.59	0.28	-666.02
		*CO	-655.2	0.16	0.29	-655.33

Supplementary Table 10. Calculated bond lengths and the Bader charge.

Sample	l_{Zn-N} (Å)	Bader charge (e)					
		PD-N	N1	N2	N3	N4	Zn
PD-Zn-N_4-1-with curvature	1.951/1.909	-1.19	-1.30	-1.30	-1.28	-1.27	1.13
PD-Zn-N_4-1-without curvature	1.964/1.915	-1.39	-1.26	-1.26	-1.31	-1.31	1.14

The labeling of sites is shown in Figure S33.

References

[1] F. Yang, P. Song, X. Liu, B. Mei, W. Xing, Z. Jiang, L. Gu, W. Xu, *Angew. Chem. Int. Ed.* **2018**, *57*, 12303-12307.

[2] J.-J. Shi, X.-M. Hu, M. R. Madsen, P. Lamagni, E. T. Bjerglund, S. U. Pedersen, T. Skrydstrup, K. Daasbjerg, *ACS Applied Nano Materials* **2018**, *1*, 3608-3615.

[3] X.-M. Hu, H. H. Hval, E. T. Bjerglund, K. J. Dalgaard, M. R. Madsen, M.-M. Pohl, E. Welter, P. Lamagni, K. B. Buhl, M. Bremholm, M. Beller, S. U. Pedersen, T. Skrydstrup, K. Daasbjerg, *ACS Catal.* **2018**, *8*, 6255-6264.

[4] K. Jiang, S. Siahrostami, T. Zheng, Y. Hu, S. Hwang, E. Stavitski, Y. Peng, J. Dynes, M. Gangisetty, D. Su, K. Attenkofer, H. Wang, *Energy Environ. Sci.* **2018**, *11*, 893-903.

[5] X. Wang, Z. Chen, X. Zhao, T. Yao, W. Chen, R. You, C. Zhao, G. Wu, J. Wang, W. Huang, J. Yang, X. Hong, S. Wei, Y. Wu, Y. Li, *Angew. Chem.* **2018**, *130*, 1962-1966; *Angew. Chem. Int. Ed.* **2018**, *57*, 1944-1948.

[6] H. B. Yang, S.-F. Hung, S. Liu, K. Yuan, S. Miao, L. Zhang, X. Huang, H.-Y. Wang, W. Cai, R. Chen, J. Gao, X. Yang, W. Chen, Y. Huang, H. M. Chen, C. M. Li, T. Zhang, B. Liu, *Nat. Energy* **2018**, *3*, 140-147.

[7] F. Pan, H. Zhang, K. Liu, D. Cullen, K. More, M. Wang, Z. Feng, G. Wang, G. Wu, Y. Li, *ACS Catal.* **2018**, *8*, 3116-3122.

[8] Y. Pan, R. Lin, Y. Chen, S. Liu, W. Zhu, X. Cao, W. Chen, K. Wu, W.-C. Cheong, Y. Wang, L. Zheng, J. Luo, Y. Lin, Y. Liu, C. Liu, J. Li, Q. Lu, X. Chen, D. Wang, Q. Peng, C. Chen, Y. Li, *J. Am. Chem. Soc.* **2018**, *140*, 4218-4221.

[9] Y.-N. Gong, L. Jiao, Y. Qian, C.-Y. Pan, L. Zheng, X. Cai, B. Liu, S.-H. Yu, H.-L. Jiang, *Angew. Chem.* **2020**, *132*, 2727-2731; *Angew. Chem. Int. Ed.* **2020**, *59*, 2705-2709.

[10] J. Han, P. An, S. Liu, X. Zhang, D. Wang, Y. Yuan, J. Guo, X. Qiu, K. Hou, L. Shi, Y. Zhang, S. Zhao, C. Long, Z. Tang, *Angew. Chem.* **2019**, *131*, 12841-12846; *Angew. Chem. Int. Ed.* **2019**, *58*, 12711-12716.

[11] W. Ren, X. Tan, W. Yang, C. Jia, S. Xu, K. Wang, S. C. Smith, C. Zhao, *Angew. Chem.* **2019**, *131*, 7046-7050; *Angew. Chem. Int. Ed.* **2019**, *58*, 6972-6976.

[12] Y. Cheng, S. Y. Zhao, H. B. Li, S. He, J. P. Veder, B. Johannessen, J. P. Xiao, S. F. Lu, J. Pan, M. F. Chisholm, S. Z. Yang, C. Liu, J. G. Chen, S. P. Jiang, *Appl. Catal. B: Environ.* **2019**, *243*, 294-303.

[13] H. Yang, Q. Lin, C. Zhang, X. Yu, Z. Cheng, G. Li, Q. Hu, X. Ren, Q. Zhang, J. Liu, C. He, *Nat. Commun.* **2020**, *11*, 593.

[14] B. Zhang, J. Zhang, J. Shi, D. Tan, L. Liu, F. Zhang, C. Lu, Z. Su, X. Tan, X. Cheng, B. Han, L. Zheng, J. Zhang, *Nat. Commun.* **2019**, *10*, 2980.

[15] J. Fu, H. Bao, Y. Liu, Y. Mi, Y. Qiu, L. Zhuo, X. Liu, J. Luo, *Small* **2020**, *16*, 1905825.

[16] H. Yang, Y. Wu, G. Li, Q. Lin, Q. Hu, Q. Zhang, J. Liu, C. He, *J. Am. Chem. Soc.* **2019**, *141*, 12717-12723.

[17] L. Lin, H. Li, C. Yan, H. Li, R. Si, M. Li, J. Xiao, G. Wang, X. Bao, *Adv. Mater.* **2019**, *31*, 1903470.

[18] S. Ren, D. Joulié, D. Salvatore, K. Torbensen, M. Wang, M. Robert, C. P. Berlinguette, *Science* **2019**, *365*, 367.

[19] T. T. Zheng, K. Jiang, N. Ta, Y. F. Hu, J. Zeng, J. Y. Liu, H. T. Wang, *Joule* **2019**, *3*, 265-278.

[20] F. Li, A. Thevenon, A. Rosas-Hernández, Z. Wang, Y. Li, C. M. Gabardo, A. Ozden, C. T. Dinh, J. Li, Y. Wang, J. P. Edwards, Y. Xu, C. McCallum, L. Tao, Z.-Q. Liang, M. Luo, X. Wang, H. Li, C. P. O'Brien, C.-S. Tan, D.-H. Nam, R. Quintero-Bermudez, T.-T. Zhuang, Y. C. Li, Z. Han, R. D. Britt, D. Sinton, T. Agapie, J. C. Peters, E. H. Sargent, *Nature* **2020**, *577*, 509-513.

Author Contributions

Mingwei Fang designed the experiments and performed the characterization. Xingpu Wang, Xueyan Li, Ying Zhu, Guozheng Xiao, Jingjing Feng, Xiaohui Jiang and Kuilin Lv analyzed the data. All authors analyzed the results and wrote the manuscript.